Materials Science and Engineering B 313 (2025) 117966

Contents lists available at ScienceDirect

Materials Science & Engineering B

journal homepage: www.elsevier.com/locate/mseb

Electrochemical sensor for catechol detection: Leveraging ITO@TiO_2/RGO/Pt nanocomposites for enhanced water quality monitoring

Rimsha Larik [a], Aamna Balouch [a,*], Esra Alveroğlu Durucu [b], Hulya Silah [c], Abdullah [d], Muhammad Saqaf Jagirani [e], Muhammad Yaqoob soomro [a]

[a] National Centre of Excellence in Analytical Chemistry, University of Sindh, Jamshoro 76080, Pakistan
[b] Department of Physics Engineering, I.T.U Faculty of Science and Letters, 34469 Maslak/Istanbul, Turkey
[c] Department of Chemistry, Faculty of Art & Science, Bilecik Seyh Edebali University, 11210 Bilecik, Turkey
[d] Tokat Gaziosmanpasa University, Faculty of Science and Arts, Chemistry Department, 60250 Tokat, Turkey
[e] Institute of Chemistry, Dalian University of Technology, Dalian, Liaoning, P.R.C., 116024, China

ARTICLE INFO

Keywords:
Environmental pollution
ITO@TiO2RGO Pt
Catechol
Electrochemical sensor
Reduced Graphene oxide-based
Nanocomposites

ABSTRACT

Recent advancements in sensor technology have led to the development of an ITO@TiO_2/RGO/Pt nanocomposite-based electrocatalyst for the detection of catechol (1,2-dihydroxybenzene) in water. Catechol is a harmful contaminant affecting human and aquatic life through polluted water and food. The nanocomposites were characterized using UV–Vis, FT-IR, FESEM, EDX, XRD, BET, zeta potential, and particle size analysis to evaluate their functionalities, morphology, composition, and surface properties. ITO glass was modified with these nanocomposites via the drop-casting method. Electrochemical characterization, including cyclic voltammetry and impedance spectroscopy, indicated optimal sensor performance with a scanning rate of 100 mV/s and pH 7 PBS, displaying a strong catechol response. The sensor demonstrated a linear range of 5–105 μM with limits of detection (LOD) and quantification (LOQ) of 0.013 and 0.046 μM, respectively, and recovery rates between 97.1 % and 101.3 % in water samples. It achieved over 7,580 turnovers with a TOF of 97.5 $(mol\ Catalyst)^{-1}\cdot(min)^{-1}$, though the TOF decreased to 34.45 after multiple uses.

1. Introduction

Pollutants in the environment are threatening the ecosystem. The aquatic environment is the final destination of almost all forms of industrial, pharmaceutical, and other pollutants, which have enormous adverse effects on living beings [1,2]. Catechol, also referred to as pyrocatechol or 1,2-dihydroxybenzene, is one of the industrial pollutants that is widely used in commercial items, including pesticides, flavors, and fragrances [3]. Catechol is broadly used in the production of photographic developers [4], as a developer for fur dyes, as an intermediate for antioxidants in rubber, pharmaceuticals [5], cosmetics, textiles, the petrochemical industry, and so on [6]. While human skin contact with it leads to eczematous dermatitis. Absorption through the skin in humans produces an illness similar to that caused by phenol, albeit with more pronounced convulsions. In animals, substantial catechol doses can induce central nervous system depression and a prolonged elevation in blood pressure, likely attributed to peripheral vasoconstriction [7,8]. Although catechol can reach the human body through various routes, including drinking water and aquatic foods, its presence in natural water sources poses a serious health risk, and developed countries have implemented strict regulations to prohibit its use in certain products. It is now necessary to keep a close eye on the amount of catechol present in the aqueous environment, particularly in drinking water. Catechol is toxic to the liver, central nervous system, and can disrupt DNA replication. Additionally, it poses a major risk to human and environmental health globally [9].

Therefore, developing methods to detect catechol concentrations is crucial for environmental safety. For catechol analysis [10], several analytical methods are frequently employed, such as spectrophotometry [11], chromatography [12], and biosensors [13,14]. These techniques, while accurate and precise, are labor-intensive, time-consuming, and require expensive equipment. For example, the analytical procedures they employ can be costly, time-consuming, and ineffective for on-site detection of specific contaminants. They also require the use of trained professionals and rigorous sample preparation. A greater number of researchers are becoming interested in Catechol analysis by

* Corresponding author at: National Centre of Excellence in Analytical Chemistry, University of Sindh (76080), Jamshoro, Sindh, Pakistan.
E-mail address: aamna_balouch@yahoo.com (A. Balouch).

https://doi.org/10.1016/j.mseb.2024.117966
Received 22 August 2024; Received in revised form 29 November 2024; Accepted 26 December 2024
Available online 7 January 2025

electrochemical techniques (EC) because of their high sensitivity, good periodic controllability, and extensive dynamic range [15,16]. Due to their on-site pollution detection at extremely low concentrations and their ease of use, electro-analytical technologies have been extensively used throughout recent decades. Over time, researchers have developed several strategies to overcome the widespread challenge of maintaining the selectivity and stability of electrochemical methods. The transfer of charge between an electrode surface and a solid or liquid phase is known as electrochemistry. Numerous types of electrochemical methods can be categorized into four basic classes: conductometric, voltammetric, amperometric, and potentiometric [17]. Electrochemical processes are largely dependent on the working electrode, and the type of electrode determines the selectivity, efficiency, and repeatability of the described method. In recent years, various analyses have presented numerous standard types of electrode materials—such as gold, platinum, graphite, carbon paste, glassy carbon, and conductive polymers as relevant electrochemical sensors. When choosing an electrode, the most important factors to consider are cost, electrical conductivity, chemical stability, activity toward the analyte, and wide potential range. Indium Tin Oxide (ITO) is a commonly used electrode in various fields of research. Based on low capacitive and electrochemical background current, wide working potential range, stable physical and electrochemical properties, commercial availability, and easy surface modification, ITO is a better working electrode compared to traditional metal electrodes commonly used for electroanalytical determinations. ITO materials also have excellent electrical conductivity and remarkable optical transparency [18].

1.1. ITO as an ideal electrode material

ITO electrodes have many advantages, such as biocompatibility, high physical and electrochemical firmness, very low background currents and low surface electrical resistance, also uncomplicated chemical modification. In addition to these, compared to other generally utilized traditional electrode materials such as carbonaceous materials, GCE, carbon, carbon fiber electrodes, boron-doped diamond (BDD), gold, screen printed electrode (SPE); ITO electrodes have a very low cost. For that reason, these electrodes have been noted as ideal electrode materials in the electrochemical techniques [18–20].

In a study conducted by Soomro et al. on the electrochemical determination of captopril, CuO-modified GCE and ITO electrodes were used as electrodes and these electrodes were named GCE/CuO and ITO/CuO, respectively. In the study, the charge transfer coefficient (α) value for both electrodes was calculated from the Tafel slopes obtained from the rising part of the measured cyclic voltammograms, and this value was obtained as 0.83 for the ITO/CuO electrode, while it was calculated as 0.73 for the GCE/CuO electrode. The α value obtained for ITO/CuO is relatively higher than that for GCE/CuO. In this case, it shows that various molecules have more oxidation susceptibility on the ITO electrode surfaces [21].

Currently, specialists have focused on building a series of customized electrodes that would provide enhanced electrocatalytic activity toward analyte detection. A lot of research work has been done to create sensors using different electrodes such as ITO, glassy carbon electrode (GCE), carbon paste electrode (CPE), and Au electrodes. Modified ITO electrodes can be used to create sensitive sensors with properties identical to those obtained with modified GCE, CPE, or other functional electrodes [19,22].

However, the research presented here provides specifics of the modifications and applications associated with this ITO electrode as a working electrode in the field of electrochemistry. Here we demonstrate the electrochemical utility of modified ITO electrodes for the detection of the organic contaminant catechol. The strategies involve modifying materials that are used as the base electrode, such as graphene-based materials, nanostructures of metals and metal oxides, carbon nanotubes, etc [23]. The exceptional properties of graphene-based materials, such as their high electrical conductivity, low weight, great chemical and thermal durability, and low toxicity, have garnered a lot of attention in recent decades. Graphene, along with its derivatives, is one of the most intriguing substances of the twenty-first century because of its properties [24,25]. Graphene oxide (GO), reduced graphene oxide (rGO), Graphene quantum dots (GQD), graphene nanoplatelets (GnP), and various other kinds are examples of graphene derivatives. Materials based on Graphene have been widely employed for electrochemical sensing applications owing to their exceptional physical and electrochemical properties. Many carbon-based materials are currently in use to improve electrode sensitivity, especially chemically modified electrochemical sensing probes based on graphene [26].

As a result, this study involves the intercalation of titanium dioxide into reduced graphene oxide (RGO) nanosheets through a modified polyol technique. The purpose is to eliminate residual oxygen and introduce significant defects on the RGO sheet surface. Moreover, the titanium dioxide becomes attached to the RGO sheets in a +4 oxidation state, facilitated by defects. This bonding enhances the charge transfer kinetics of RGO, improves its electro-catalytic properties, and results in the decoration with platinum metal that is ultimately attached to an indium tin oxide glass sheet. The main objective of the modified polyol method is to incorporate titanium dioxide-based reduced graphene oxide decorated with platinum metal and accommodate the glass sheet of indium tin oxide. Nonetheless, pure TiO_2 is not a particularly good absorber, RGO and Pt metal are present in its layers, which promote absorption.

The resultant reduced graphene oxide (RGO) exhibits superior conductivity, increased surface area, and outstanding electrocatalytic characteristics compared to pristine GO. The incorporation of titanium dioxide on the RGO surface, adorned with platinum metal and attached to an indium tin oxide glass sheet, plays a crucial role in facilitating the electro-oxidation of catechol. This is attributed to the active participation of titanium dioxide in its +4 oxidation state in the electrochemical reaction.

In addition, it is well known that indium tin oxide (ITO) electrodes can be used as an electrochemical sensing platform due to their wide potential window and stable electrochemical properties [27]. Furthermore, compared to glassy carbon electrodes (GCE), ITO is a cost-effective material and more suitable for mass production and practical application, which is accustomed to being used as the substrate for fabricating disposable sensors, such as H_2O_2, glucose, and hydrazine sensors. To the best of our knowledge, however, the preparation of ITO@TiO_2/RGO/Pt modified electrode by the modified polyol process for electrochemical sensing has never been reported so far [28].

To our knowledge, this marks the inaugural application of titanium dioxide as a functionalizing agent in the RGO sheets decorated with platinum nanocomposites to accommodate the glass sheet of indium tin oxide as (ITO@TiO_2/RGO/Pt) achieved through a modified polyol process. This dual role serves to enhance the electrochemical properties. This leads to the creation of an electro-catalytic material with high sensitivity, specifically engineered for precise catechol detection in real-world samples.

2. Experimental design

2.1. Preparation of materials

Ultrapure Milli-Q water was utilized as the sole solvent in the entire experiment. All glassware was soaked in an acidic solution for 24 h and then washed with distilled water and rinsed with deionized water. Later, the glassware was dried at 100 °C in the oven before use in the experiment. An Indium tin oxide substrate (ITO) (size 1 × 1.5 cm) with a sheet resistance of approximately 9–22 Ω^{-2} was used.

2.2. Materials and Chemicals

Indium tin oxide substrate was purchased from Vinkarola, USA with a purity of > 99 %. Graphite powder (purity ≥ 99 %) and nitric acid (HNO_3) (purity ≥ 69 %), sulfuric acid (H_2SO_4) (purity ≥ 98 %), sodium nitrate ($NaNO_3$) (purity ≥ 99 %), hydrochloric acid (HCl) (purity ≥ 37 %), sodium chloride (NaCl) (purity ≥ 99 %), potassium chloride (KCl) (purity ≥ 99 %), magnesium sulfate ($MgSO_4$) (purity ≥ 99 %), acetophenone ($C_6H_5COCH_3$) (purity ≥ 99 %) and 5 wt% Nafion® perfluorinated resin solution were purchased from Merck (Germany). Standards of ascorbic acid ($C_6H_8O_6$) (purity ≥ 99 %), hydroquinone ($C_6H_6O_2$) (purity ≥ 99 %), benzoquinone ($C_6H_4O_2$) (purity ≥ 99 %), salicylic acid ($C_6H_4(OH)CO_2H$) (purity ≥ 99 %), uric acid ($C_5H_4N_4O_3$) (purity ≥ 99 %), and catechol ($C_6H_6O_2$) (purity ≥ 99 %) were purchased from Sigma-Aldrich. Titanium salt tetraisopropoxide ($Ti[OCH(CH_3)_2]_4$) (purity ≥ 98 %), isopropanol (CH_3CH_2CHOH) (purity ≥ 99 %), sodium dodecyl sulfate ($CH_3(CH_2)_{11}SO_4$ Na) (purity ≥ 98 %), methanol (CH_3OH) (purity ≥ 99 %), and ethanol (CH_3CH_2OH) (purity ≥ 99 %) were obtained from Dae-Jung (China). Phosphate-buffered saline (PBS) (purity ≥ 98 %), potassium hydroxide (KOH) (purity ≥ 98 %), borate-buffered saline (BBS), and Briton-Robinson (BRB) buffers were prepared as 0.1 M solutions in deionized water. For acidic and basic media, 0.1 M HCl and NaOH, respectively, were used to adjust the pH of the supporting electrolytes.

2.3. Synthesis of reduced graphene oxide and TiO_2/RGO/Pt nanocomposites

Reduced graphene oxide (RGO) was synthesized from graphite powder using the modified Hummers' method [29]. The noble metal TiO_2/RGO/Pt nanocomposites were synthesized via the modified polyol process. For the synthesis of Pt-doped TiO_2/RGO nanocomposites (TiO_2/RGO/Pt), the TiO_2/RGO composite was first suspended in ethylene glycol (EG). A 0.005 M solution of the Pt precursor (K_2PtCl_6) and TiO_2/RGO composite in a 1:2 ratio was dissolved in EG, and ultrapure Milli-Q water was added slowly under magnetic stirring. The solution was refluxed in a two-necked round-bottom flask equipped with a heating mantle and subjected to magnetic stirring at 100 °C for 3 h. Subsequently, the resulting solid was thoroughly washed with ultrapure Milli-Q water multiple times and retrieved by centrifugation (6000 rpm, 30 min). See Fig. 1 for the preparation of TiO_2NPs, RGO, TiO_2/RGO Composites, and TiO_2/RGO/Pt Nanocomposites which are described below.

2.4. Fabrication of ITO@TiO_2/RGO/Pt nanocomposites sensor

The bare electrode was modified with ITO@TiO_2/RGO/Pt

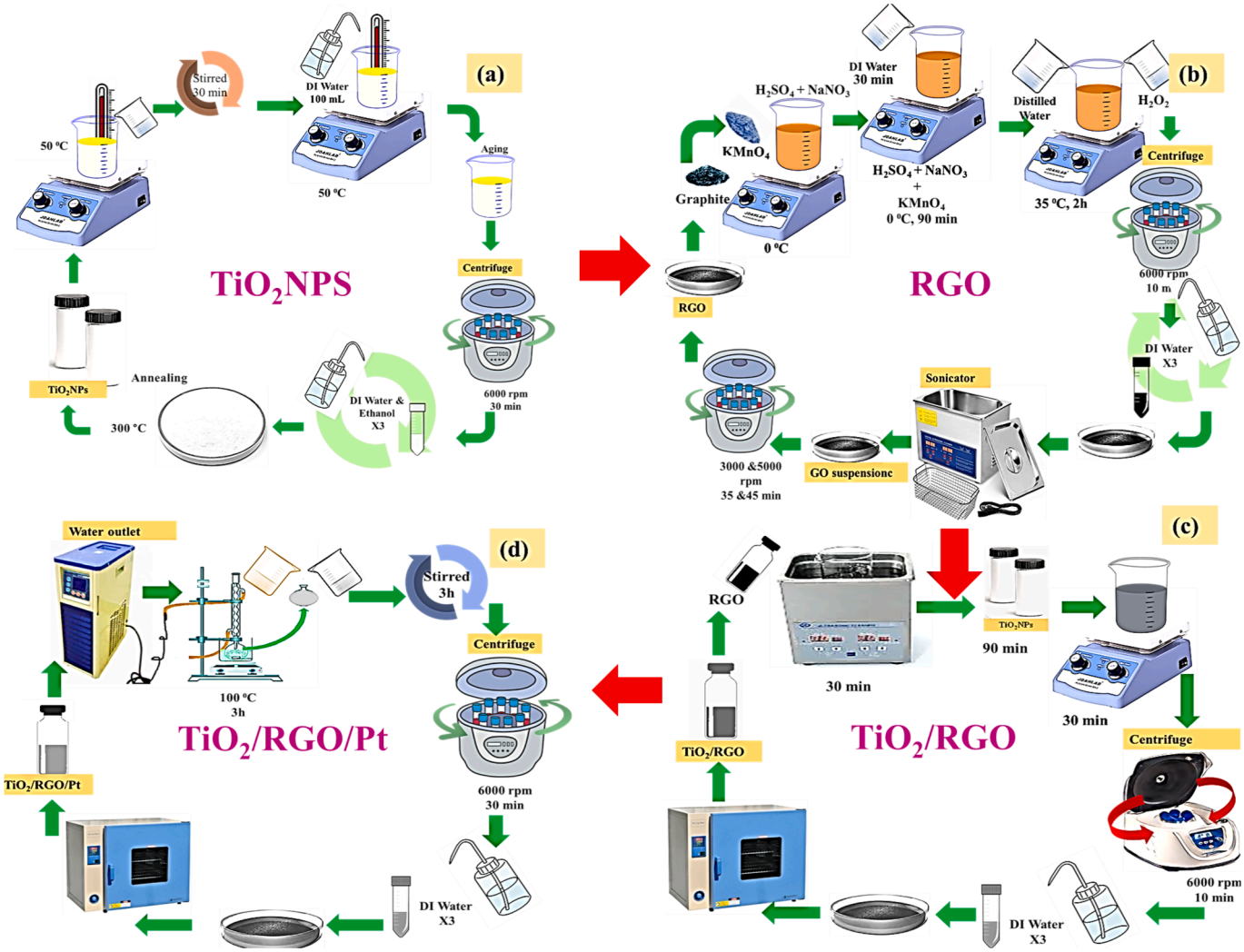

Fig. 1. Overview of Four Different Synthesis Processes. This figure illustrates the following synthesis processes: (a) Titanium Dioxide Nanoparticles (TiO_2NPs), (b) Reduced Graphene Oxide (RGO), (c) Fabrication of TiO_2/RGO Composite, and (d) Formation of TiO_2/RGO/Pt Nanocomposites. Each process is depicted with its corresponding steps for clarity.

nanocomposites using a slightly modified drop-casting technique [30]. To formulate the modified electrode, dissolve 5 mg of the prepared TiO_2/RGO/Pt nanocomposites in 2.5 mL of deionized water, followed by the addition of 50 μL of Nafion solution as a binding agent. After a half-hour of ultrasonication, a homogeneous suspension of the TiO_2/RGO/Pt nanocomposites and Nafion was achieved. Following a deionized water cleaning, the ITO glass sheet surface was sonicated for half an hour in a 30 mL ethanol solution. Finally, a 5 μL solution of the TiO_2/RGO/Pt nanocomposites was applied to the ITO glass sheet surface to form ITO@TiO_2/RGO/Pt, and the electrode was allowed to dry for 20 min at room temperature.

2.5. Data collection and analysis

Data collection involved measuring the electrochemical performance of the ITO@TiO_2/RGO/Pt nanocomposite sensor under controlled environmental and experimental conditions. To comprehensively evaluate the TiO_2/RGO/Pt nanocomposites, a series of analytical techniques were employed, each providing a detailed understanding of their structural and functional properties. UV–Vis spectroscopy provided insights into the optical characteristics and band gap, while FTIR spectroscopy elucidated the presence of functional groups and chemical bonds. The crystalline structure was analyzed using X-ray diffraction (XRD), and the Brunauer-Emmett-Teller (BET) method quantified surface area and porosity, both essential for catalytic efficiency. Energy Dispersive X-ray Spectroscopy (EDX) further detailed the elemental composition and distribution within the nanocomposites. Stability and dispersion were assessed through zeta potential and particle size analysis, ensuring the nanocomposites were suitable for electrochemical applications. The electrochemical performance of the fabricated ITO@TiO_2/RGO/Pt nanocomposite electrodes was meticulously evaluated using a CHI electrochemical workstation configured in a three-electrode setup. Here, cyclic voltammetry (CV) was employed at a scan rate of 100 mV/s in a 0.1 M KCl solution with 5 mM redox probes, revealing critical information about conductivity, charge transfer resistance, and overall electrochemical kinetics. The resulting data, including peak current densities and electrochemical impedance, were analyzed to establish correlations between the material properties and their electrochemical performance, highlighting the potential of the TiO_2/RGO/Pt nanocomposites for advanced applications.

3. Results and discussion

3.1. The U.V visible analysis

After preparing the TiO_2/RGO/Pt nanocomposites, their properties were analyzed using a UV–visible spectrophotometer (Biochrom Libra S22). Initially, Initially, the UV–vis spectrum of the as-prepared TiO_2 nanoparticle solution, synthesized via the hydrolysis method using isopropyl alcohol and deionized (DI) water, was recorded. The maximum absorption peak for the formulated TiO_2 NPs was achieved at 257 nm, as shown in Fig. 2a. The intensity and position of the peaks are similar to

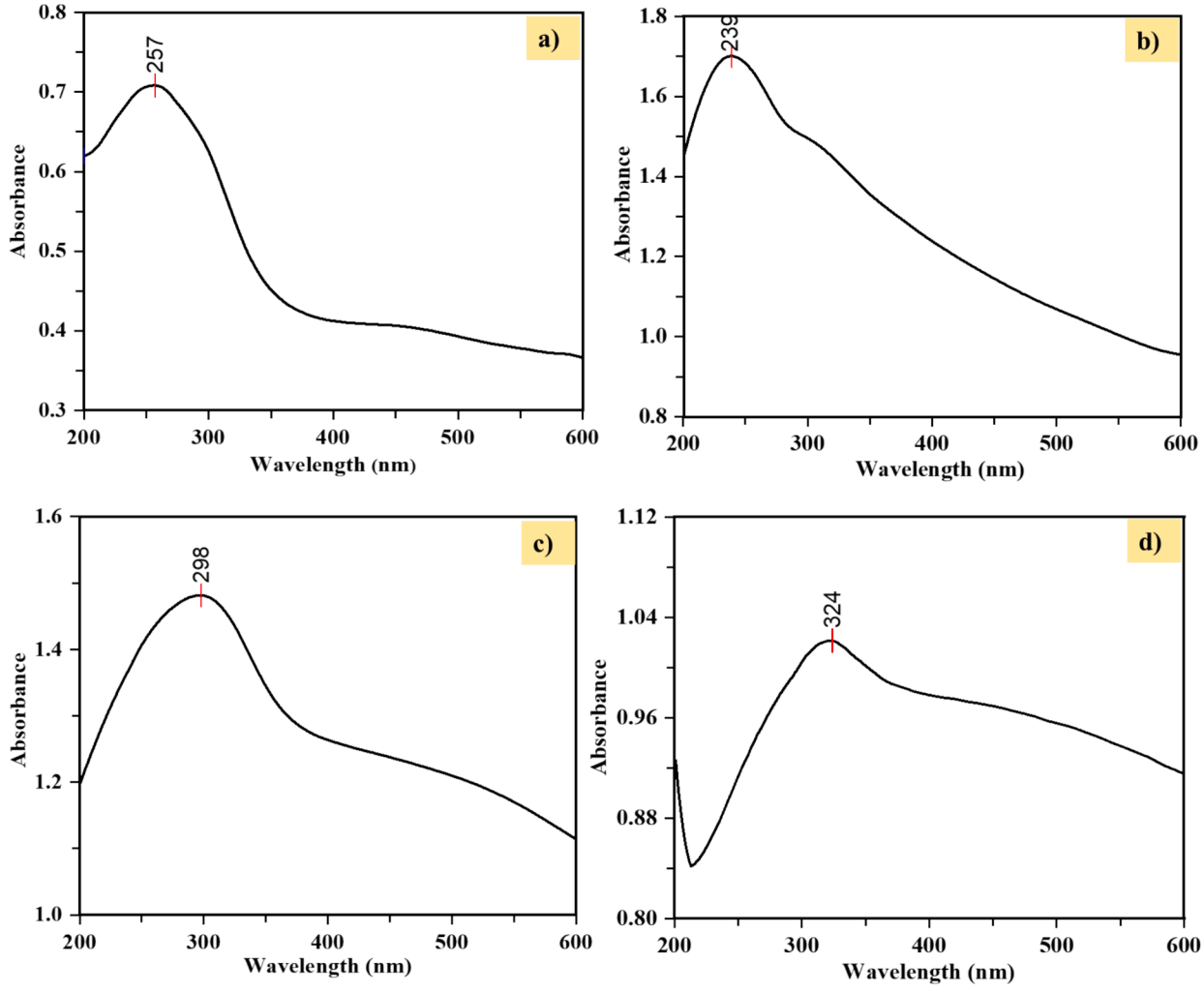

Fig. 2. UV–Visible spectrum of (a) TiO_2 NPs (b) RGO (c)TiO_2 /RGO Composite (d) TiO_2 /RGO/Pt Nanocomposites.

those reported in earlier studies [31], and the nanoparticles were found to be highly stable. This is consistent with the findings of other TiO_2-based systems, where similar absorption peaks in the UV range have been reported [1,2].

The RGO nanosheets were synthesized using a modified Hummers method. The maximum absorption peak for the formulated RGO was achieved at 239 nm. This is quite similar to the work reported by [32], where the absorption peak was observed at 238 nm. The strong absorption peak at 239 nm was attributed to the π–π* transitions of graphitic C–C bond interactions [31,32]. The prepared RGO was found to be highly stable, as shown in Fig. 2b.

Next, the TiO_2/RGO composite material was synthesized using a modified single-step colloidal blending technique. The maximum absorption peak for the formulated TiO_2/RGO composite was observed at 298 nm. The position of the peaks is similar to the previously published work [33], where the absorption peak was observed at 310 nm. This phenomenon might be the result of increased clumping of RGO sheets and surface aggregation of TiO_2NPs. The effective absorption of visible light promises greater efficiency in utilizing sunlight for photocatalytic activity. The formation of Ti-O-C chemical bonds in the composites can be attributed to prolonged visible light absorption, which is further supported by FT-IR and XRD analyses, as illustrated in Fig. 2c.

Finally, the UV–vis spectrum of the prepared TiO_2/RGO/Pt nanocomposites, synthesized via a modified polyol process, was recorded. The maximum absorption peak for the TiO_2/RGO/Pt nanocomposites was observed at 324 nm, placing it in the near-UV region (200–400 nm). The addition of precious metals further improves the optical characteristics of the TiO_2/RGO composite. We believe that the precious metal nanoparticle insulation of TiO_2 from light limits the amount of photoelectrons that are produced and raises band gap energy, as illustrated in Fig. 2d.

3.2. Band gap energy

A plot of $(\alpha h\nu)^2$ versus photon energy ($h\nu = 1239/\lambda$) is shown in Fig. 3. This indicates that the band gap of pure TiO_2 is 3.20 eV [34], while that of pure RGO is 2.7 eV. The band gap of TiO_2/RGO composites has decreased to 2.5 eV, and the band gap of TiO_2/RGO/Pt nanocomposites has decreased further to 2.2 eV. The band gap energy is calculated from the UV–visible absorption spectrum of the materials using the Tauc plot method. The UV–visible spectrum provides information about how much light the material absorbs at different wavelengths, and the corresponding photon energy ($h\nu$) is given by the equation $h\nu = 1239/\lambda$, where λ is the wavelength in nanometers and $h\nu$ is the photon energy. The Tauc plot involves plotting $(\alpha h\nu)^2$ versus photon energy ($h\nu$), where α is the absorption coefficient. The band gap energy (Eg) is determined from the linear portion of the plot, where the x-intercept of the extrapolated line corresponds to the optical band gap. This method allows the extraction of the band gap from the absorption characteristics in the UV–visible range, where electronic transitions typically occur in semiconductors and nanocomposites. The absorption in the UV–visible range reflects how the material interacts with light and reveals the energy required to excite electrons from the valence band to the conduction band, which corresponds to the optical band gap. In the case of materials like RGO (Reduced Graphene Oxide), TiO_2/RGO composites, and TiO_2/RGO/Pt nanocomposites, each material has a distinct absorption spectrum, reflecting its unique electronic structure; the band gap energy is then derived from these spectra using the Tauc plot. Investigations into the impact of oxidation time variation on the electrical, physical, and chemical properties of reduced graphene oxide (RGO) revealed that the bandgap of RGO grew as the amount of oxygen in the RGO material increased [35]. RGO is adjustable in the visible spectrum between 1.9 and 2.6 eV, which is necessary for effective photocatalysis. Its bandgap ranges from 1.7 to 4.3 eV depending on the

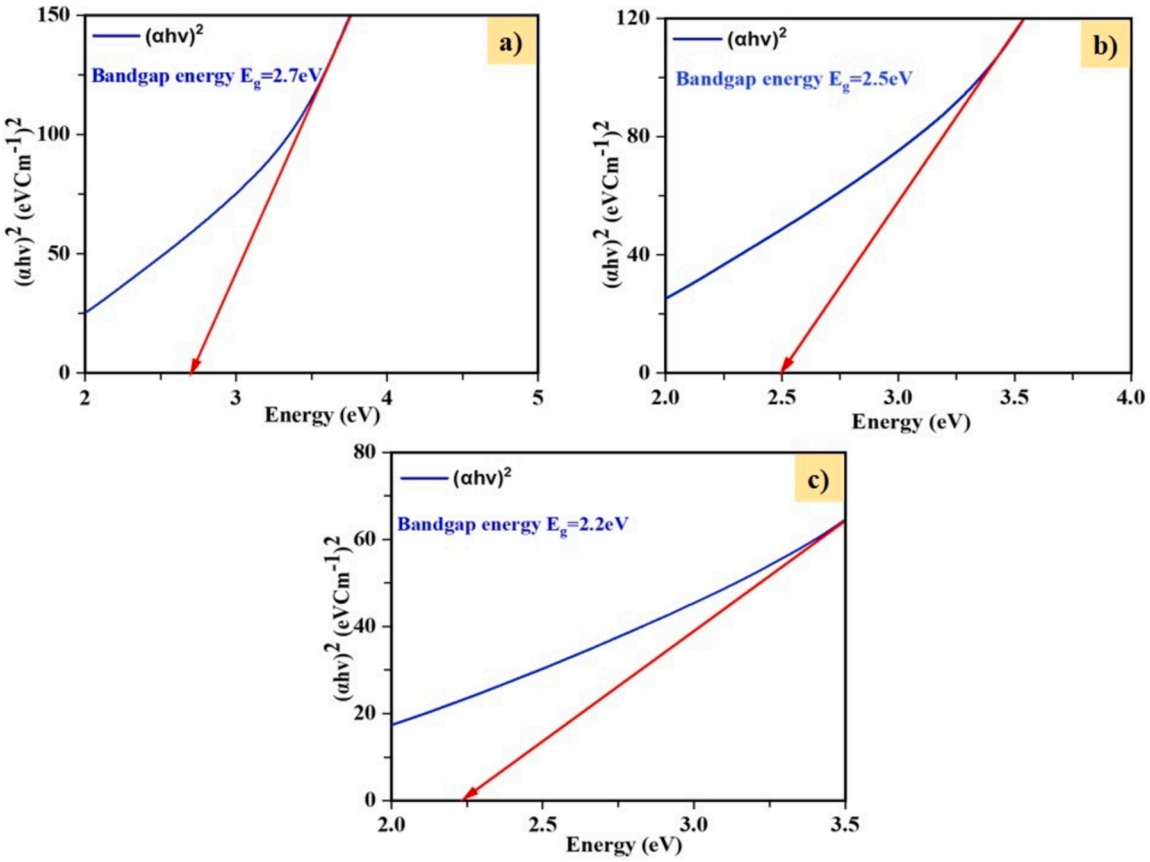

Fig. 3. Band gap energy of (a) RGO (b) TiO_2 /RGO Composite (c) TiO_2 /RGO/Pt Nanocomposites.

preparation technique. The non-stoichiometric substance graphene oxide maintains the graphite lamellar structure. Numerous oxygen-containing groups, including carboxyl (C − OOH), hydroxyl (C − OH), and epoxide (C − O − C), become covalently bonded to the surfaces of its layers after treatment in the presence of strong acids and oxidizing agents. In our experiment, in the presence of the Ti-peroxo-complex, RGO reacted, and some functional groups on the RGO surface, such as (–OH, –COOH), were eliminated. The formation of a Ti–O–C structure raises the valence band edge and narrows the band gap. This can be explained by the bonding of unpaired electrons with free electrons on the surface of TiO_2 [36]. However, after photoactivation of titanium dioxide photoactivation, electrons may readily migrate to graphene nanosheets, and photoinduced holes can migrate into titania; this results in a considerable reduction in e^- and h^+ recombination, which raises the process yield.

3.3. The FT-IR analysis

FT-IR spectroscopy was used to study the functionalities in the synthesized TiO_2/RGO/Pt nanocomposites in the range of 4000–400 cm^{-1}. Various functional groups and surface interactions were identified using the FT-IR instrument (PerkinElmer Spectrum Two). Fig. 4 presents the FT-IR spectra of TiO_2NPs, RGO, TiO_2/RGO composite, and TiO_2/RGO/Pt nanocomposites. The strong peak at 3440 cm^{-1} corresponds to the hydroxyl (OH) functional group, which is due to the surface absorption of water on the material [33]. Meanwhile, the medium band at 2943 cm^{-1} is attributed to the asymmetric stretching of the C–H bond, resulting from the inclusion of isopropanol in the TiO_2 NPs, TiO_2/RGO, and TiO_2/RGO/Pt nanocomposites [37,38]. In the case of composite formation, a new adsorption band was observed. The absorption band of bare TiO_2 and RGO at 2943 cm^{-1} (black and red line) shifts to 2860 cm^{-1} (blue line), confirming the changes attributed to symmetrical C–H stretching. The bands at 1728 cm^{-1}, 1705 cm^{-1}, and 1624 cm^{-1} correspond to the stretching vibration of carboxyl C=O, C-O, and C=C in the synthesized TiO_2/GO composites, respectively [36]. Meanwhile, the minor peak at 1497 cm^{-1} is due to C–O carboxy stretching [39]. The peak at 1436 cm^{-1} corresponds to the Ti-O-C bond [33]. The peaks spanning from 1389 cm^{-1} correspond to C-OH stretching vibrations [40]. While the medium peak obtained at 1386 cm^{-1} shows the stretching and bending of the C–H bond due to the presence of isopropyl alcohol. The Ti-O-C linkage is present, as indicated by the tiny signal at 1081 cm^{-1} [33]. The broad peaks at 1064 cm^{-1}and1053 cm^{-1} are attributed to the C-O stretching vibration of the alkoxy group [41]. The peak at 640 cm^{-1} is related to a combined signal due to Ti-O-Ti and Ti-O-C linkage. The Ti-O stretching in TiO_2 suggests the structure of TiO_2 after

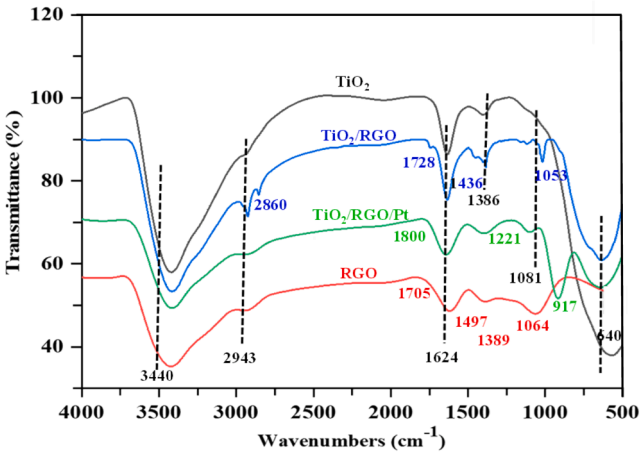

Fig. 4. FTIR spectra of TiO_2 NPs, RGO, TiO_2 /RGO Composite, and TiO_2 /RGO/Pt Nanocomposites.

it has been treated with temperature and indicates the highly active anatase phase of TiO_2 [33,42,43]. In the case of TiO_2/RGO/Pt nanocomposites formation, a new absorption band was observed. The absorption band of bare RGO and TiO_2/RGO composite at 1705 cm^{-1} and 1728 cm^{-1} (red and blue line) is shifted to 1800 cm^{-1} (green line), which confirms the changes that are attributed to the C–H bend [36].

The absorption band of bare RGO and TiO_2/RGO composite at 1389 cm^{-1} and 1386 cm^{-1} (red and blue line) is due to Alcoholic C-O–H and epoxide C–O–C or C-O–H is shifted to 1221 cm^{-1} (green line), which confirms the changes that are attributed to the C-OH or C-O-C stretching [44]. In addition, nanocomposites presented high peaks at 917 cm^{-1} that were attributed to the stretching vibrations of Ti-O-Ti and Ti-O-C bonds. Therefore, the above results confirmed the successful Preparation of TiO_2/RGO composites and TiO_2/RGO/Pt nanocomposites via a modified polyol process.FTIR spectra of TiO_2/RGO/Pt nanocomposites do not show any bands corresponding to those noble metals due to the low loading of deposited metal. The most straightforward and prevalent approach used to verify the successful production of nanoparticles is UV–visible spectroscopy. Under standard lab conditions, the freshly synthesized material was operated by choosing a wavelength between 200 and 400 nm. As apparent from the mentioned figure, the TiO_2/RGO/Pt exhibits a prominent absorption band around 324 nm.

3.4. Surface analysis

The advanced FESEM analysis provides a stunning visual insight into the surface morphology of our synthesized material—TiO_2, RGO, RGO-TiO_2, and RGO-TiO_2@Pt—detailed in Fig. 4a–f, using the Field Emission Scanning Electron Microscope (FESEM EOL JSM 7000F) technique.

The pristine TiO_2 nanoparticles exhibit a strikingly uniform, cube-like tablet structure, showcasing their well-defined crystalline nature, as shown in Fig. 5a According to Wang et al., the growth of TiO2 thin film is anatase form[45]. This three-dimensional arrangement underlines the exceptional structural integrity of TiO_2.

The FESEM images of the as-prepared reduced graphene oxide (RGO) are shown in Fig. 4b to illustrate its surface morphology. The FESEM images offer a high-resolution perspective of the structural properties of RGO. One characteristic that sets graphene-based materials apart is the pronounced sheet-like shape observed in pristine RGO. These sheets, typical of reduced graphene oxide, are large, flat, and irregularly shaped. The shrinkage of these sheets is a distinctive observation made in the images. The reduction process, which usually comprises the removal of oxygen-containing groups from the oxide graphene and results in a more condensed structure, maybe the cause of this shrinkage. The surface area and overall properties of RGO are influenced by its sheet-like structure and the observed shrinking. The surface morphology of synthesized material TiO_2 decorated with RGO nanosheets TiO_2/RGO Composite, FESEM imaging vividly captures the uniform distribution of TiO_2 cube-like tablets across the RGO sheets, forming seamlessly integrated composites with a well-aligned nanoscale interaction Fig. 5c–d, this clear depiction affirms the successful formation of the GO-TiO_2 composites, highlighting the homogeneity and effective synergy between TiO_2 and GO.

Turning to the GO-TiO_2@Pt nanocomposites, the FESEM analysis reveals an intriguing surface morphology: TiO_2 tablets are elegantly enveloped by multilayer reduced graphene oxide sheets. The platinum nanoparticles (Pt NPs) exhibit a spherical, textured appearance and are evenly distributed across both the reduced graphene oxide surfaces and between the layers of RGO. This comprehensive coverage and uniform decoration of platinum NPs are demonstrated in Fig. 5e–f, confirming the successful integration of TiO_2 with reduced graphene oxide and the effective decoration with platinum nanoparticles. Overall, the FESEM images provide compelling evidence of the successful synthesis and structural evolution of these nanocomposites, underscoring their potential for advanced applications.

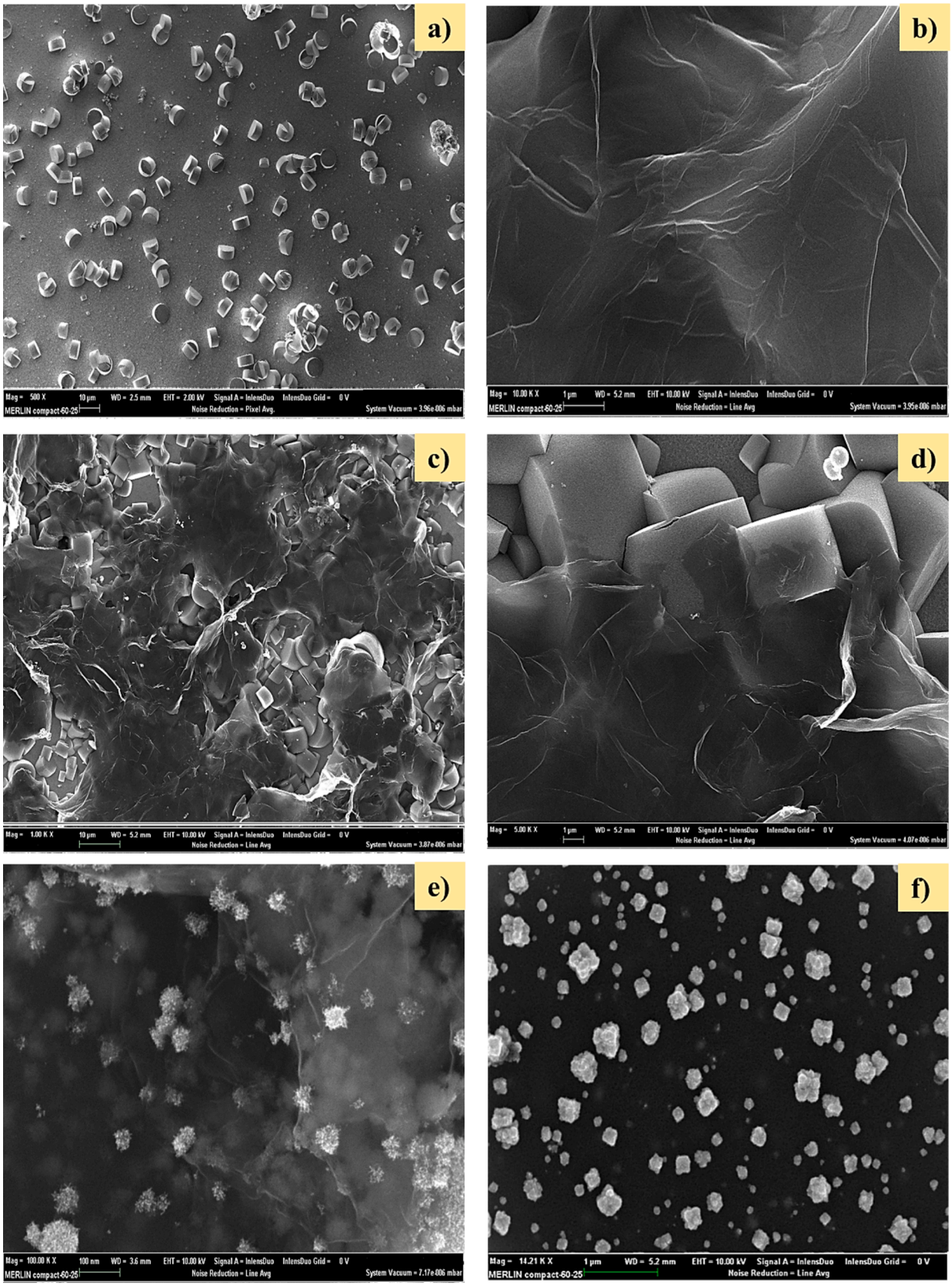

Fig. 5. FESEM images showcasing the morphology of different materials: (a) Titanium Dioxide Nano Tablets (TiO_2), (b) Reduced Graphene Oxide (RGO), (c-d) TiO_2/RGO Composite at low and high resolution, and (e-f) TiO_2/RGO/Pt Nanocomposites at low and high resolution.

3.5. Elemental analysis or chemical characterization

The energy dispersive X-ray (EDX) examination was carried out to evaluate the elemental composition of the materials. EDX spectra analysis further confirms the presence of carbon, oxygen, titanium, and platinum elements in the fabricated nanocomposites. The EDX spectra were found to be impurity-free, which confirms the exceptional purity of the prepared material. The EDX spectra of RGO are displayed in Fig. 6a. Moreover, the carbon–oxygen percentages in RGO were noted as 62.84 % and 37.16 % without any other impurities. The EDX spectrum of the fabricated TiO_2/RGO Composite is shown in Fig. 6b. The EDX spectrum confirms the presence of carbon, oxygen, and titanium in the synthesized TiO_2/RGO Composite. The carbon–oxygen and titanium were 17.09 %, 26.39 %, and 46.34 %, respectively, in the prepared TiO_2/RGO Composite, which confirmed the successful preparation of the TiO_2/RGO composite. The EDX spectrum of the fabricated TiO_2/RGO/Pt Nanocomposites is shown in Fig. 6c. By the proposed modified polyol method, TiO_2 is incorporated into the RGO sheet decorated with platinum metal nanocomposites very well. The percentage of carbon–oxygen in titanium and platinum was 11.64 %. Oxygen significantly decreased to 22.18 %, and platinum was 22.11 %, which is a clear evidence of the successful fabrication of TiO_2/RGO/Pt Nanocomposites.

3.6. Phase structure and crystallinity confirmation

X-ray Diffraction (XRD) frequently provides details on the crystalline structure, phase composition, lattice parameters, and crystalline grain size. The crystalline nature was confirmed through the application of the X-ray diffractometry MMA (GBC Scientific Equipment, Australia) model. By comparing the peak locations and intensities to reference patterns from the JCPDS database, the ICDD was able to estimate the particle composition. The XRD peaks are too broad for tiny particles. Hence, it is not appropriate for amorphous materials. TiO_2/RGO/Pt nanocomposites (a), platinum metal (b), TiO_2/RGO composites (c), TiO_2 nanoparticles (d), and RGO (e) had their X-ray diffraction patterns examined by XRD spectroscopy (Fig. 7a), XRD diagram of the naked nanocomposites displayed the spinel titania pattern.

These strong peaks, observed at (101), (004), (200), (105), (211), (204), (220), (002), (111), (311), and (222), correspond to the face-centered cubic structure of the highly crystalline TiO_2/RGO/Pt nanocomposites. Anatase TiO_2 results were confirmed by the (JCPDS NO. 21–1272), which states that the prepared material is crystalline in nature, smaller in size, and has a tetragonal crystal structure. The intense pattern at (002) confirms the successful Preparation of RGO, and results were also confirmed by the (JCPDS NO. 75–2078). Whereas, the broad XRD pattern at (111), (200), (220), (311), and (222) suggest the excellent crystallinity of Pt metal, and results were also confirmed by the (JCPDS NO. 04–0802) that describes prepared material with face-centered cubic structure. The stability of the crystalline phase of TiO_2 nanoparticles during reduced graphene oxide coating was shown by the same sets of characteristic peaks for TiO_2/RGO composites (c) confirmed by previous research. Furthermore, no impurities were visible in any of the diffraction patterns, indicating that the prepared TiO_2/RGO/Pt nanocomposites were highly pure. This observation confirms the strong chemical interaction between the TiO_2/RGO composites and platinum (Pt) metal to form the TiO_2/RGO/Pt nanocomposites. Additionally, the Debye-Scherrer formula was used to determine the size of the TiO_2/RGO/Pt nanostructure; the average crystal size was 27.6 nm.

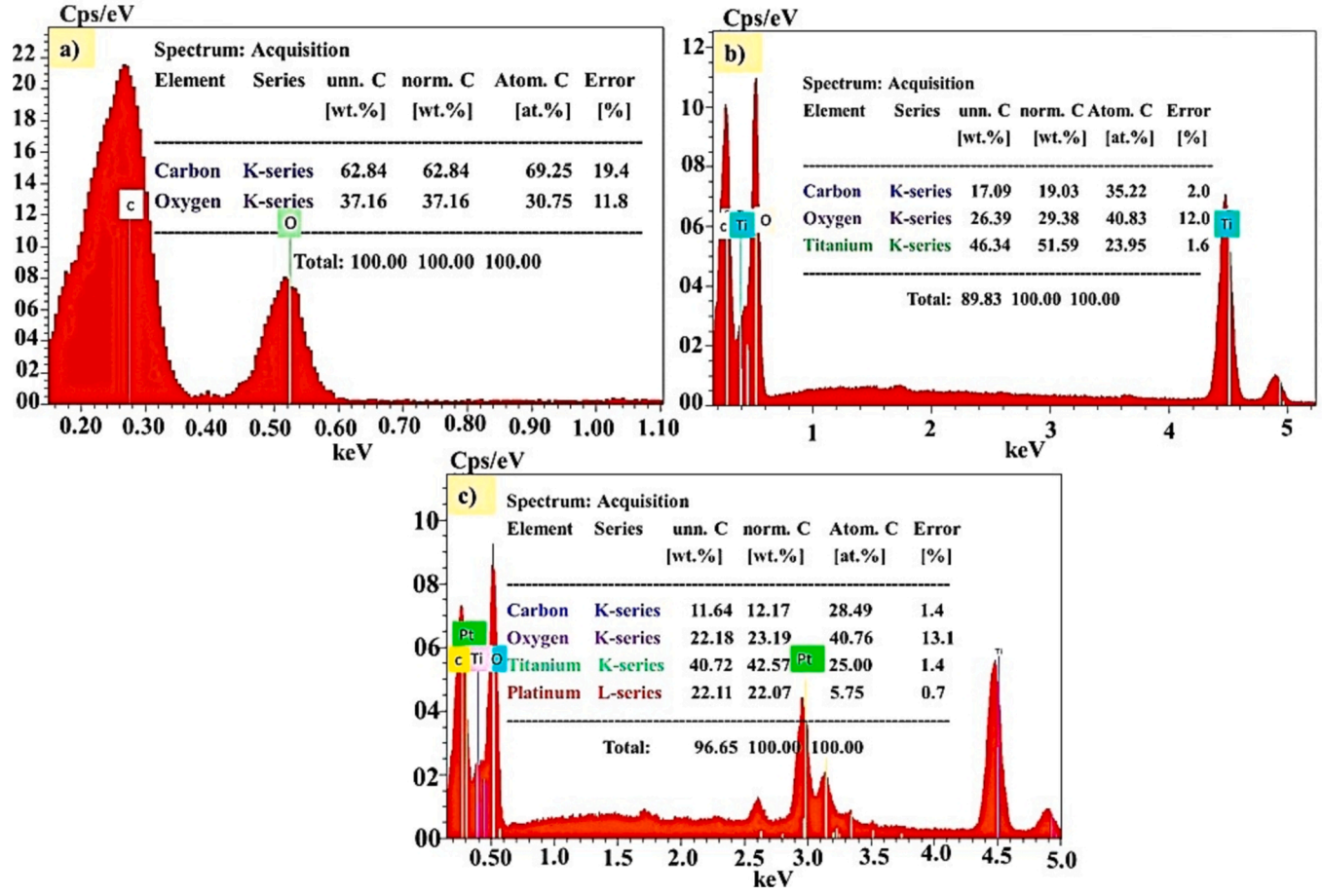

Fig. 6. EDX Spectra of (a) RGO (b) TiO_2 /RGO Composite (c) TiO_2 /RGO/Pt Nanocomposites.

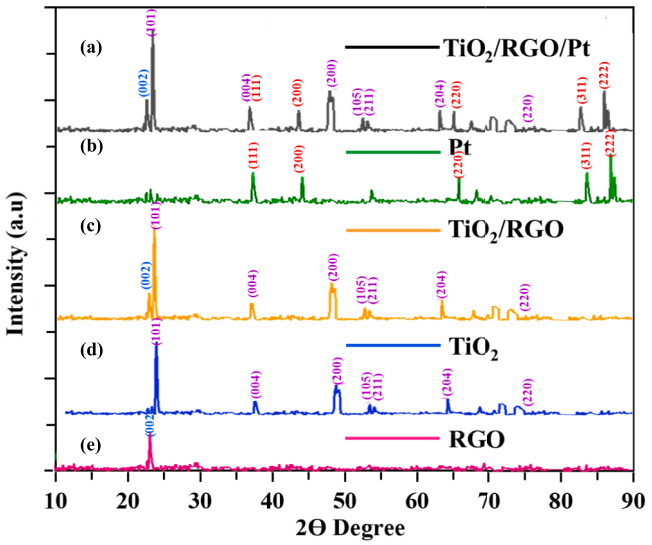

Fig. 7. XRD patterns illustrating the phase composition of various materials: (a) TiO_2/RGO/Pt Nanocomposites, (b) Platinum (Pt) Metal, (c) TiO_2/RGO Composite, (d) Titanium Dioxide Nanoparticles (TiO_2 NPs), and (e) Reduced Graphene Oxide (RGO).

3.7. Zeta potential analysis

The Melvern Instrument enables Zeta potential, which analyses the surface charge of nanoparticles in a colloidal solution using (Zetasizer Ver. 7.11 MALVAREN) technology. Fig. 8a presents the zeta potential analysis of RGO through the application of zeta sizer technology; the surface potential of the produced material was assessed. The surface potential and stability of the produced materials were verified using the potential mode. One of the most challenging tasks to address to present novel chemical and physical properties is the precise control of particle size and particle size distribution. The RGO surface has a high charge, which enhances dispersion stability. Large zeta values for the synthesized RGO (−33.4 mV) indicate that they are more stable in aqueous solutions. This and the work mentioned by [46,47] are very similar.

Additionally, this shows that the RGO nanosheets resisted one another and did not flocculate [48,49]. A key parameter that shows if nanosheets are stable, is the zeta potential is in the limit of ±30 mV [50]. The negatively charged surfaces of RGO distributed in water are seen at neutral pH.

Fig. 8b presents the zeta potential analysis of the TiO_2/RGO Composite. Due to their distinctive characteristics, transition metal composites have attracted a lot of interest as potentially advanced catalysts. The composite surface has a high charge, which enhances dispersion stability. The TiO_2/RGO Composite that had been produced exhibited significant zeta values (−25.4 mV), which indicated that it was more stable in aqueous solutions. This and the research that [51] reported are fairly comparable.

Additionally, this shows that the composite repels each other and does not flocculate [48,49]. The key parameter that shows if a composite is stable, is the zeta potential is in the limit of ±30 mV. The negatively charged surface of the TiO_2/RGO Composite in water is seen at neutral pH.

Fig. 8c presents the zeta potential analysis of TiO_2/RGO/Pt Nanocomposites. Transition metals, due to their distinctive characteristics, nanocomposites have been actively researched as potentially enhanced

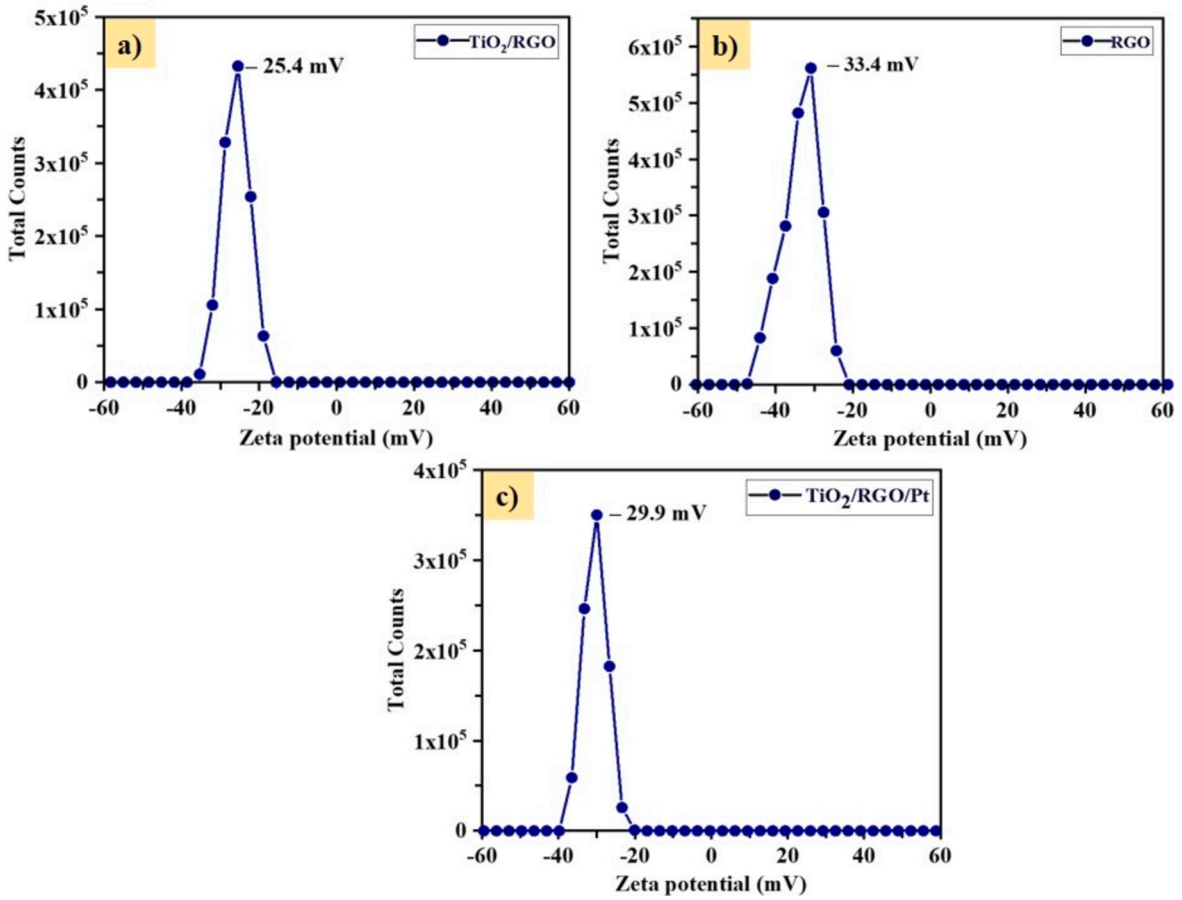

Fig. 8. Zeta potential of (a) RGO (b)TiO_2 /RGO Composite (c) TiO_2 /RGO/Pt Nanocomposites.

catalysts. One of the most challenging tasks to resolve to provide unique chemical and physical properties is the precise control of particle size and particle size distribution. The nanocomposite surface is highly charged, which enhances dispersion stability. The TiO_2/RGO/Pt nanocomposites that had been produced exhibited significant zeta values (−29.9 mV), which indicated that it was more stable in aqueous solutions.

Additionally, this shows that the composite repels each other and does not flocculate [48,49]. The key parameter that shows if a nanocomposite is stable, is the zeta potential is in the limit of ±30 mV. The negatively charged surface of the TiO_2/RGO/Pt nanocomposites in water is seen at neutral pH.

3.8. Zeta sizer analysis

The dispersed powdered sample of synthesized Reduced graphene oxide nanosheets was examined to reveal the size distribution. The Malvern Instrument enables the size of nanoparticles using (Zetasizer Ver. 7.11 MALVAREN) technology. The TiO_2NPs suspension size distribution was measured by dynamic light scattering (DLS) measurement at 458 nm with a scattering angle was 90 degrees. Due to their distinctive properties, transition metal nanoparticles have received considerable interest as potentially advanced catalysts. One of the most challenging tasks in providing unique chemical and physical properties is the precise control of particle size and particle size distribution. The details of the zeta sizer of Fig. 9 are given in supplementary information S3.8. The size distribution of the prepared RGO nanosheet suspension was measured in a complete medium as determined by DLS measurement at the scattering angle of 90 degrees. DLS employed standard spherical particle models. A size of 531 nm for the prepared RGO was recorded. The results we obtained correlate with those of [52], who found that the size of RGO had a size distribution observable at 525 nm. Most graphene-based materials are not spherical particles; DLS results only show the size of the material.

The dispersed powdered sample of the composite made from reduced graphene oxide-based titanium dioxide was examined to reveal the size distribution in DI water at neutral pH, which was attributed to the development of TiO_2/RGO aggregates. RGO nanosheets and TiO_2NPs were combined using ultrasonic mixing to create TiO_2/RGO composites with high particle sizes. The size distribution of the prepared TiO_2/RGO suspension was measured in a complete medium as determined DLS measurement was found at 164 nm. The position of the peaks is in proximity to the earlier published work [53], where the size distribution was observed at 220 nm.

The dispersed powdered sample of Titanium dioxide-based reduced graphene oxide nanosheet decorated with platinum nanocomposites was analyzed to disclose the size distribution in DI water at neutral pH, which was ascribed to the formation of TiO_2/RGO/Pt aggregates. The size distribution of the prepared TiO_2/RGO/Pt suspension was measured in a complete medium as determined by DLS measurement. The size of the prepared nanocomposites was found to be 122.4 nm. Most reduced graphene-based materials are not spherical particles. Due to their distinctive properties, transition metal nanoparticles have received considerable interest as potentially advanced catalysts. One of the most challenging tasks to resolve to provide unique chemical and physical properties is the precise control of particle size and particle size

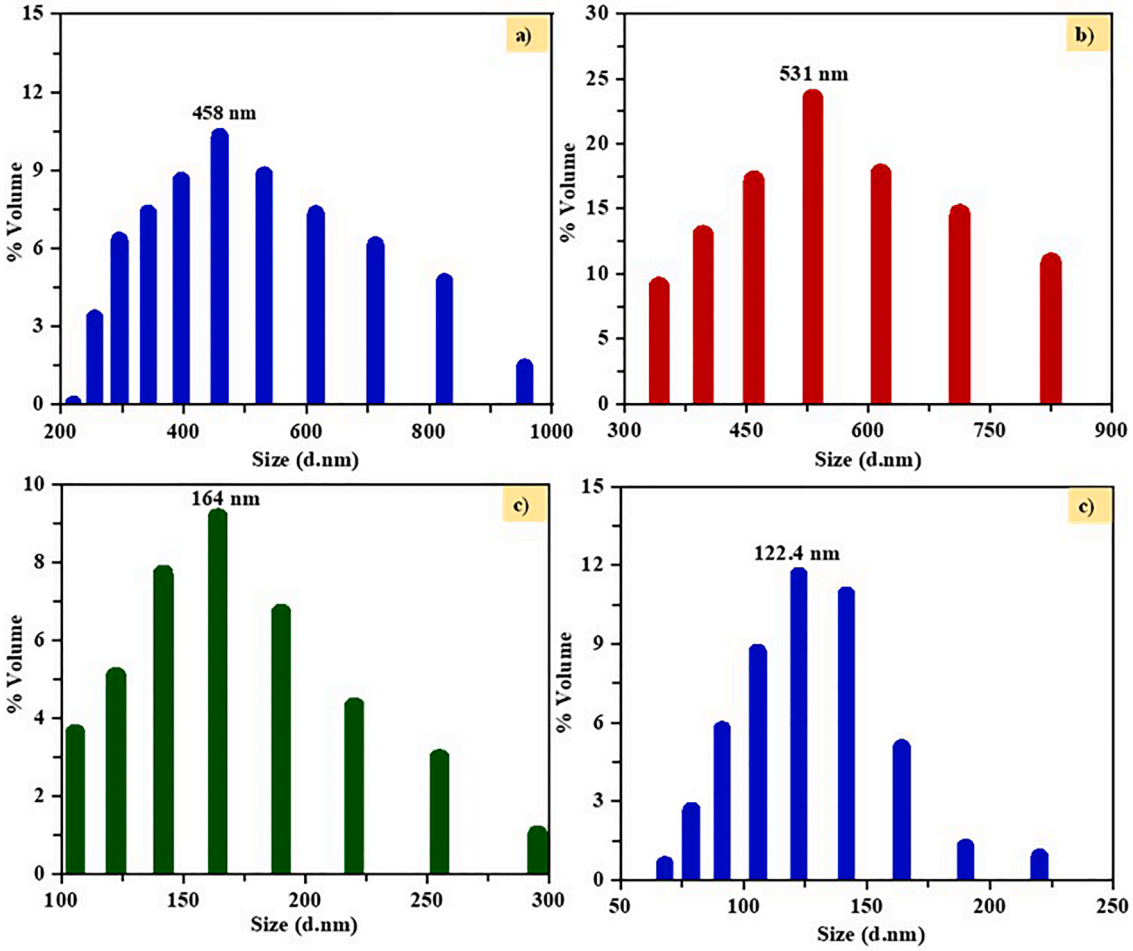

Fig. 9. Zeta Size analysis of (a) RGO, (b) TiO_2/RGO composite, (c) TiO_2/RGO/Pt Nanocomposite.

distribution. DLS results only show the size of the material.

3.9. Surface area and porosity measurements

The specific surface area and pore volume of synthesized materials were determined using BET analysis with Autosorb-1 Quanta chrome and ASiQwin, as shown in Fig. 10. The nitrogen adsorption–desorption isotherms for RGO, TiO_2/RGO composites, and TiO_2/RGO/Pt nanocomposites were classified as type III according to IUPAC, indicating weak adsorbent-adsorbate interactions with H3 hysteresis loops, associated with plate-like particle aggregates forming slit-like pores [54]. The IUPAC classifies pores as microporous (<2 nm), mesoporous (2–50 nm), and macroporous (>50 nm). RGO was found to be microporous, while TiO_2/RGO and TiO_2/RGO/Pt nanocomposites were mesoporous, indicating unrestricted multilayer formation [55]. The measured specific surface areas were 2.987 m^2/g for RGO, 35.679 m^2/g for TiO_2/RGO, and 40.977 m^2/g for TiO_2/RGO/Pt. The pore size distribution curves, obtained using the BJH method, showed narrow distributions with sizes under 3 nm, confirming the mesoporous nature of the TiO_2/RGO/Pt catalyst. Table 1 details the BET surface area, average

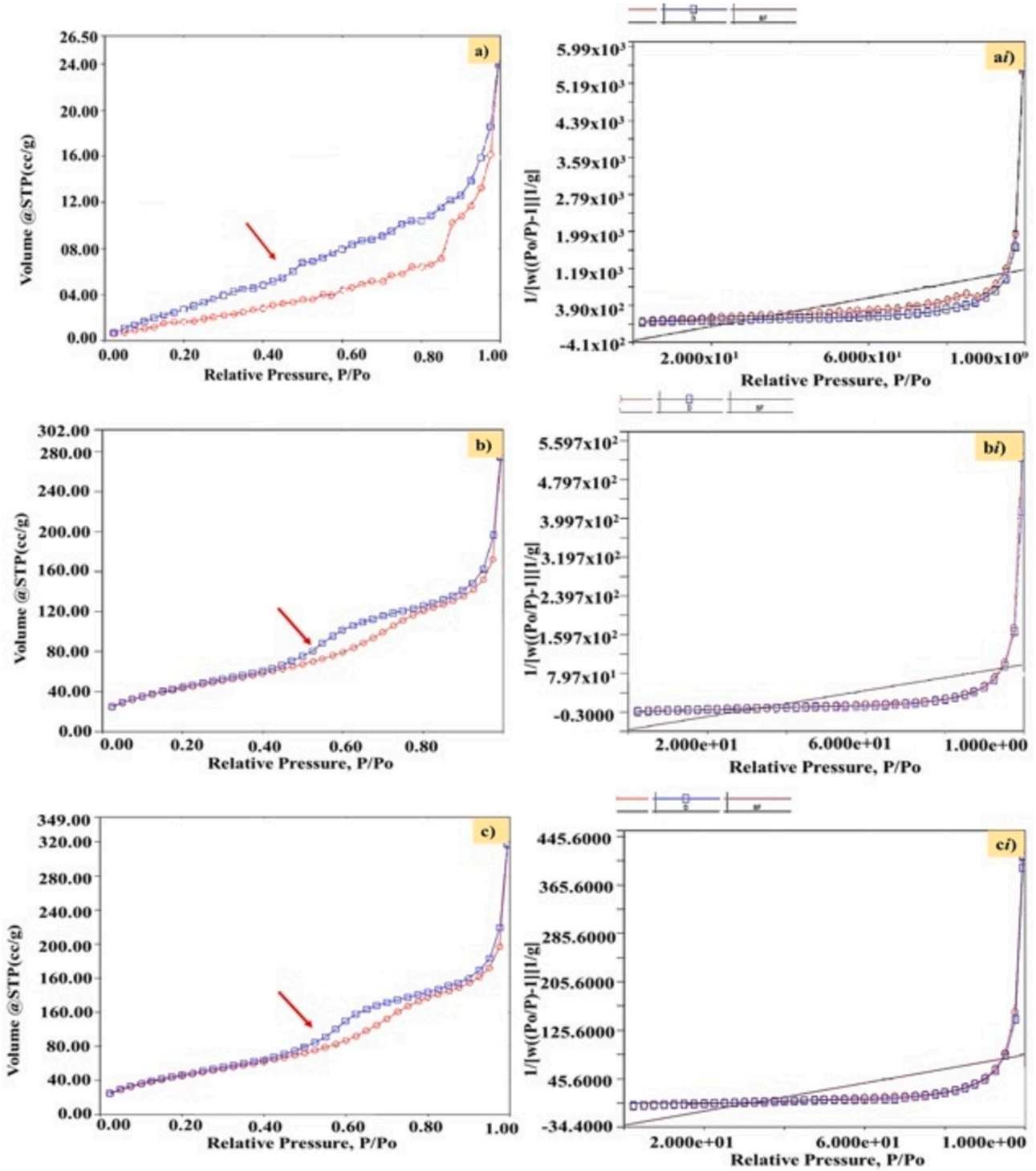

Fig. 10. BET curves and the inserted graph represent the multipoint Plot of (a) RGO,(b) TiO_2 /RGO Composite, and(c) TiO_2 /RGO/Pt Nanocomposites.

Table 1
BET surface area of RGO, TiO_2 /RGO composites, and TiO_2 /RGO/Pt nanocomposites.

Sample	Multi-point BET surface Area (m^2/g)	Adsorption			Desorption		
		Surface Area (m^2/g)	Pore Vol (cc/g)	Pore Diameter (nm)	Surface Area (m^2/g)	Pore Vol (cc/g)	Pore Diameter (nm)
RGO	2.987	9.874	0.039	1.6571	16.571	0.037	1.9646
TiO_2/RGO	35.679	59.957	0.233	2.5224	86.860	0.243	1.8513
TiO_2/RGO/Pt	40.977	116.722	0.395	2.9153	156.435	0.411	2.2115

pore size, and total pore volume for these materials.

3.10. Turnover number (TON) and turnover frequency (TOF) of the catalyst

The catalyst's efficiency was assessed through the total turnover number (TON) and turnover frequency (TOF) for catechol oxidation in an aqueous medium. TON indicates the number of reactant molecules converted to products per 5 μL of catalyst from a 5 mg TiO_2/RGO/Pt nanocomposite solution. TOF is calculated as TON divided by time. For the ITO@TiO_2/RGO/Pt catalyst with a 40 μM catechol solution, it achieved over 7,580 turnovers in 60 s, as shown in Fig. 11a. Initially, the TOF was 97.5 $(mol\ Catalyst)^{-1}\cdot(min)^{-1}$. However, with repeated use, the TOF decreased to 34.45 after multiple cycles, as shown in Fig. 11b. The catalyst was reused effectively after washing and drying, demonstrating its recyclability despite a gradual decline in performance over successive uses.

4. Electrochemical behavior of bare and modified electrodes

Cyclic voltammetry (CV) was used to assess the electrochemical characteristics and conductivity of the fabricated electrodes, using a CHI electrochemical workstation (Tennison Hill Drive, Austin, USA) with a three-electrode setup: An Indium tin oxide (ITO) glass sheet as the working electrode, platinum wire as the counter electrode, and an Ag/AgCl as the reference electrode. Electrochemical analyses were conducted at a scan rate of 100 mV/s in a solution of 0.1 M KCl with 5 mM redox probes [$K_3Fe(CN)_6$ and $K_4Fe(CN)_6$]. The bare/ITO electrode showed a consistent redox response. In contrast, the TiO_2 nanoparticles (TiO_2NPs) and reduced graphene oxide (RGO) each exhibited a very minute redox response so subtle that it was barely discernible in the graphical representation. Whereas, the ITO@TiO_2/RGO/Pt nanocomposites exhibited an enhanced redox response, indicating superior conductivity. This is illustrated in Fig. 12a, which compares the CV responses. Another, electrochemical measurement for bare and modified electrodes was investigated via electrochemical impedance spectroscopy (EIS) through a circuit-fitted Nyquist plot. The Nyquist plot revealed that the ITO@TiO_2/RGO/Pt electrode had a more favorable redox response compared to the bare electrode, demonstrating its excellent electro-catalytic performance. TiO_2 thin films, known for their chemical stability and photocatalytic activity in the UV region, were combined with reduced graphene oxide (RGO) to enhance electrochemical performance. The TiO_2/RGO/Pt nanocomposites created a large electroactive surface area, improving adsorption capacity and catalytic sites for analyte oxidation. In Nyquist plots, the charge transfer resistance is a key parameter as shown in Fig. 12b with experimental conditions set at an initial potential of 1.3 mV, high frequency of up to 100,000 Hz, low frequency of 1 Hz, and a quiet time of 2 s, confirmed the enhanced charge transfer kinetics of ITO@TiO_2/RGO/Pt. The Rct from EIS mainly relies upon the redox probe electron transfer kinetics at the surface of modified and bare/ITO electrodes, which is estimated through the diameter of the semicircle curve of the EIS response in Nyquist-plot. EIS study explains the conductive nature of charge transfer resistance of electrodes with a semicircle harmonic curve. The EIS response in the

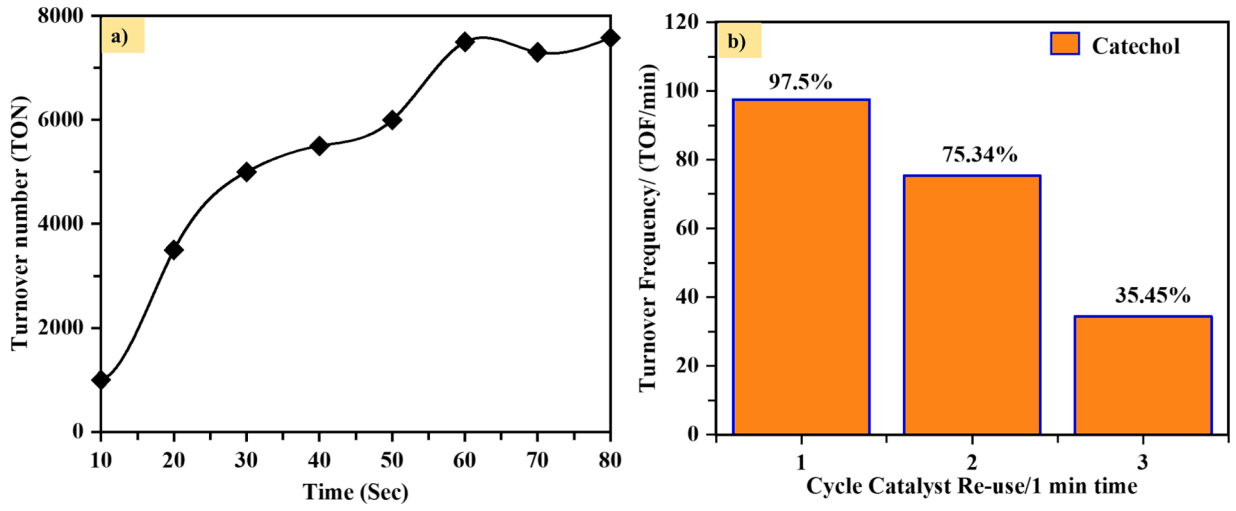

Fig. 11. (a) The Plot of turnover number versus time (b) plot of turnover Frequency versus reusability of catalyst at 1 min reaction time for the degradation of organic pollutant phenol.

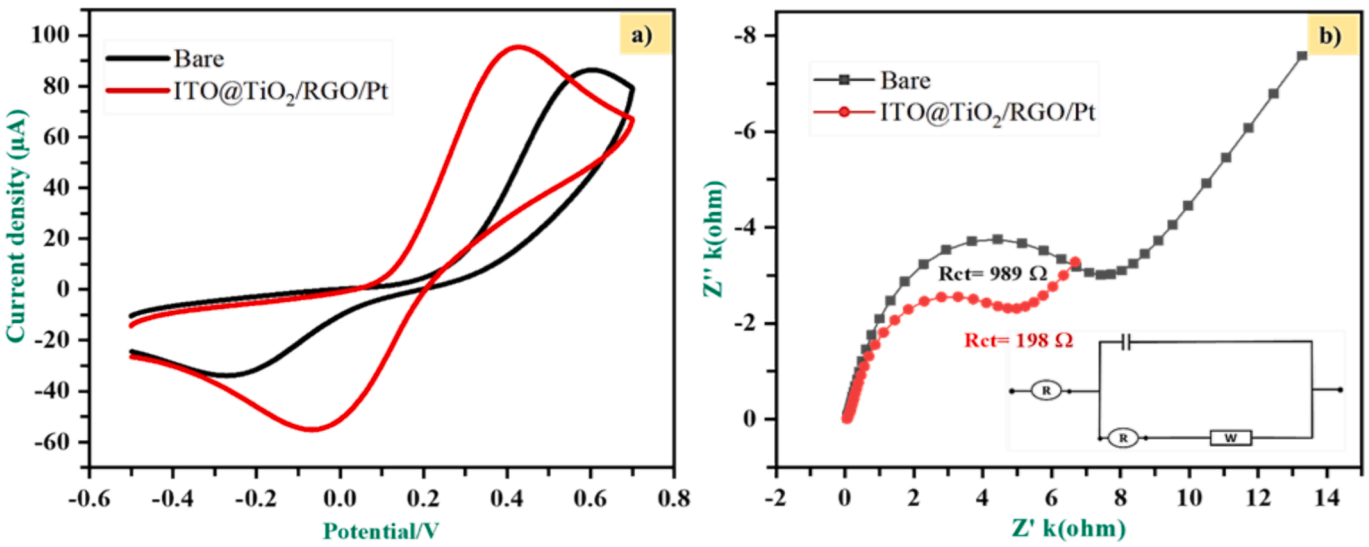

Fig. 12. (a)Cyclic voltammetry (CV) profiles of bare and modified electrodes were recorded at a scan rate of 100 mV/s in a solution containing 0.1 M KCl and 5 mM [(K_3 Fe(CN)$_6$ and K_4 Fe(CN)$_6$], (b) Electrochemical impedance spectroscopy (EIS) Nyquist plots for both bare and modified electrodes were generated at the initial potential of 1.3 mV, covering a low-frequency range of 1 and a high-frequency range of 100,000.

Nyquist plot with a narrower semicircle curve faces low possible resistance, while the broadness of the curve explains the greater resistance faced by the electrode employed under the EIS study. Herein, the broadness of the semicircle curve is monitored for the bare electrode which means the Bare/ITO electrode faces greater resistance with the Rct value calculated as (989 Ω), while the modified ITO@TiO_2/RGO/Pt one with a narrower diameter exhibits excellent conductive nature with low resistance and the Rct value was measured as (198 Ω), respectively, in the test solution. These EIS outcomes align well with the CV analysis, collectively indicating that ITO@TiO_2/RGO/Pt stands out as an effective sensing probe. From EIS results, the low possible resistance and high conductivity of the modified electrode, compared to the Bare/ITO electrode is another evidence that the ITO@TiO_2/RGO/Pt underscores the excellent performance and makes it a promising candidate for the electrochemical determination of catechol.

4.1. *Electrochemical determination of catechol*

The study aimed to develop a highly sensitive and reliable electrochemical sensor for precise catechol detection. Cyclic voltammetry (CV) was employed to analyze both bare and ITO@TiO_2/RGO/Pt electrodes in a 40 µM catechol solution with PBS as the supporting electrolyte, scanning at 100 mV/s within the range of 0.0 to 0.9 V versus Ag/AgCl. The supporting electrolyte is an important component of a voltammetric cell. The supporting electrolytes are soluble substances and theoretically, their ions have a very high ionic mobility, letting them take up the charge transport by migration on account of the electric field composed by the potential difference. Thus, migration transport is maximized to install a diffusive control in the electrochemical cell. All this is a conclusion of the truth that the current that is related to concentration in voltammetric techniques is the diffusion current, for that reason, charge and mass transport by migration and convection introduce deflections from the theoretical equations governing the redox process, which in practice results in loss of precision and accuracy of the voltammetric quantification method. For this reason, in this electrochemical study, the effects of different types of support electrolytes were investigated and the supporting electrolyte with the best desired electrochemical properties (such as showing defined plateaus, high limiting current, and lower variability) was selected. The CV results revealed that both electrodes responded to catechol, as shown in Fig. 13. The ITO@TiO_2/RGO/Pt electrode exhibited a significantly stronger redox peak, indicating

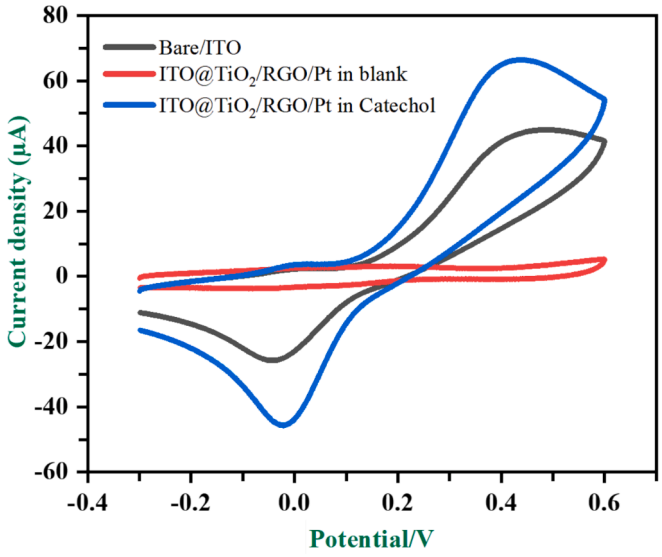

Fig. 13. CV redox peak response of bare and ITO@TiO_2 /RGO/Ptin 40 µM catechol at the scan rate of 100 mV/s in PBS electrolyte pH 7.

superior sensitivity and conductivity. Thus, the ITO@TiO_2/RGO/Pt sensor demonstrated excellent specificity and performance for catechol detection.

a. Effect of Supporting Electrolyte

The choice of supporting electrolyte is crucial in electrochemical techniques for analyte determination, as it ensures effective communication between the analyte and the electrode surface. Supporting electrolytes, which are highly soluble and possess high ionic mobility, facilitate charge transport by migration, which is essential for accurate measurements. However, deviations from theoretical redox equations due to migration and convection can affect precision and accuracy. In this study, various supporting electrolytes were tested to find the optimal one for catechol detection. The electrolytes included borate buffer (pH 8.0), BRB buffer (pH 3.0), H_2SO_4 buffer (pH 2.0), KOH (pH 10), and PBS buffer (pH 7.0) [3], adjusted with 0.1 M HCl or 0.1 M

NaOH to cover a range from acidic to basic conditions. Using an ITO@TiO_2/RGO/Pt electrode, the redox responses were measured at a scan rate of 100 mV/s. As shown in Fig. 14, PBS buffer at pH 7.0 provided the most effective redox response for 40 μM catechol. Therefore, PBS was selected as the supporting electrolyte for further measurements. The ITO glass sheet modified electrode was cleaned with deionized water and ultrasonicated in 30 mL of ethanol for 30 min before and after each measurement. This process ensured that the electrode's surface remained clean for accurate analytical detection of catechol in water samples.

b. 5 pH study and scan rate optimization

The pH of the supporting electrolyte significantly impacts the electrochemical response of analytes. Acidic pH shifts the peak potential to more positive values, while basic pH shifts it to more negative values. Optimal sensitivity occurs when the analyte exhibits maximum current response at the appropriate pH. In this study, the pH range of PBS electrolyte was varied from 5.8 (basic) to 7.4 (neutral). As shown in Fig. 15a, and Fig. 15b the pH range of PBS electrolyte was varied from 5.8 (basic) to 7.4 (neutral) the catechol anodic peak current (ipa) and cathodic peak current (ipc) called redox current increased with pH from 5.8 to 7 peaking at pH 7.4. Beyond pH 7, the current response declined, indicating that basic pH does not favor ion transformation. Therefore, PBS at pH 7 was selected for catechol detection due to its optimal proton transfer, enhancing redox response. A scan rate analysis was performed to assess the adsorption-controlled process of the ITO@TiO_2/RGO/Pt electrode. The study revealed that increasing the scan rate from 20 to 100 mV/s led to linear current responses, suggesting a diffusion-controlled mechanism. The regression equations for anodic and cathodic peak currents were $R^2 = 0.9799$ and $R^2 = 0.9632$, respectively, demonstrating linear behavior (Fig. 15c and Fig. 15d). The Randle-Sevcik equation confirms that the current response grows linearly with the scan rate, indicating a diffusion-controlled process. Randle-Sevcik states that there is a greater flow of ions from the electrolytic solutions toward the surface of the electrode as the total number of scan sweeps increases. As a result, a good electro-catalyst opposes this behavior and causes the current to grow linearly with an increase in scan rate. Additionally, Scheme 1 illustrates the catechol oxidation mechanism on the ITO@TiO_2/RGO/Pt surface, where catechol is oxidized to its quinone form [56]. The exceptional conductivity of ITO@TiO_2/RGO/Pt nanocomposites enables the oxidation reaction of the analyte.

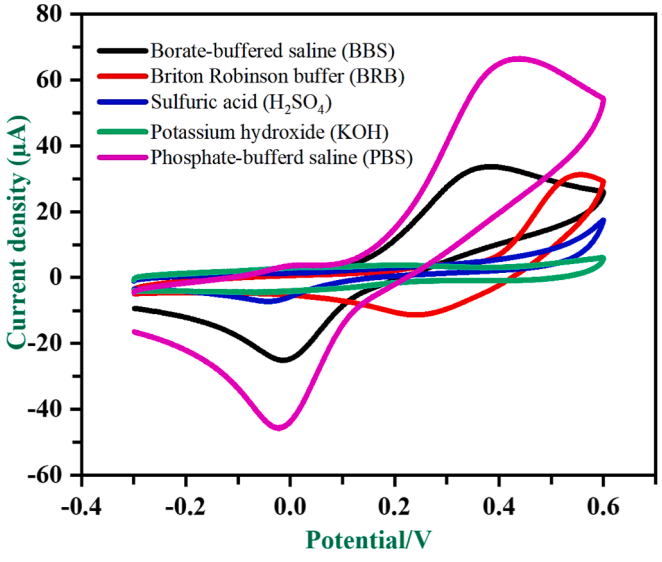

Fig. 14. CV redox peak response of ITO@TiO2/RGO/Pt in 40 μM catechol at a scan rate of 100 mV/s in PBS in different supporting electrolytes.

In the presence of the ITO@TiO_2/RGO/Pt catalyst, the oxidation of catechol to quinone unfolds as a fascinating and efficient process. The reaction begins with the carefully synthesized TiO_2/RGO/Pt nanocomposite, which acts as a powerful facilitator. When catechol ($C_6H_4(OH)_2$) is introduced into the reaction mixture, the catalyst enhances electron transfer, promoting the transformation to benzoquinone ($C_6H_4O_2$). Under controlled conditions, the catalyst generates reactive oxygen species (ROS) that further accelerate this oxidation, leading to the loss of two electrons and protons from the catechol molecule. The resulting quinone, characterized by its distinct absorption peaks in UV–Vis spectroscopy, signifies a successful reaction. This elegant interplay of materials and reactions highlights the potential of ITO@TiO_2/RGO/Pt as a catalyst in organic transformations, paving the way for advanced applications in various fields, including environmental remediation and sensor development.

$$\boldsymbol{ip} = 0.4463\boldsymbol{nFAC}\sqrt{\left(\frac{\boldsymbol{nFVD}}{\boldsymbol{RT}}\right)} \quad (1)$$

In the given context: *ip* denotes the peak current response in amperes (A), n signifies the electron transfer involved in the redox reaction, typically equal to 1, *F* represents the Faraday constant in C mol^{-1}, *A* denotes the electrode surface area in cm^2, *C* stands for concentration in mol/cm^3, *D* is the diffusion coefficient in cm^2/s, ν is the scan rate in V/s, *R* is the gas constant in $JK^{-1}mol^{-1}$, and *T* represents the temperature in K.

5.1. Effect of interferants and stability study

The selectivity of chemically modified sensors is crucial for accurate analyte detection, ensuring they respond only to the targeted substance without significant fluctuations in peak potential or current. In this study, the selectivity of the ITO@TiO_2/RGO/Pt-based sensor was evaluated by adding interferants such as acetophenone (ACP), ascorbic acid (AA), hydroquinone (HQ), benzoquinone, salicylic acid (SA), uric acid (UA), catechol, SO_4^{2-}, and NO_3^- ions at concentrations twice that of catechol. The analyte solution also included Na^+ and $Mg2^+$ ions which are potential interferants in real matrices. Catechol was tested at 40 μM and the interferants at 100 μM, using a scan rate of 100 mV/s in a pH 7 PBS electrolyte. Results, shown in Fig. 16a, indicate that the sensor exclusively responds to catechol, demonstrating excellent selectivity. Stability tests involved over 15 repeated daily cycles, with the sensor showing a relative standard deviation (RSD) of 1.52 %, indicating high stability. Fig. 16b shows that over 30 days, the sensor's inter-day stability was assessed using five cycles per day. The sensor maintained good stability for 25 days with an RSD of 4.73 %. However, after 25–30 days, the redox response decreased, with RSDs exceeding 7 %. Overall, the ITO@TiO_2/RGO/Pt sensor demonstrates outstanding stability for up to 25 days, making it highly suitable for long-term catechol analysis.

5.2. Calibration study of catechol

Differential pulse voltammetry (DPV) was employed to calibrate the ITO@TiO_2/RGO/Pt sensor for catechol detection, establishing its linear dynamic range (LDR) from 5 to 105 μM in a pH 7 PBS electrolyte at a pulse time of 100 mV/s. The sensor demonstrated an excellent linear response across these concentrations, as shown in Fig. 17a. To ensure repeatability, each DPV cycle was performed five times, with Fig. 17b illustrating the consistent redox response and peak potential. The calibration curve yielded a high regression value (R2 = 0.9974), indicating strong linearity. The limit of detection (LOD) was calculated as 0.013 μM, and the limit of quantification (LOQ) as 0.046 μM, using standard formulas. These values highlight the sensor's excellent sensitivity compared to existing methods. The ITO@TiO_2/RGO/Pt sensor proved to be more selective, economical, stable, and sensitive than previously reported sensors, as detailed in Table 2. This method offers a cost-effective and efficient approach to catechol sensing.

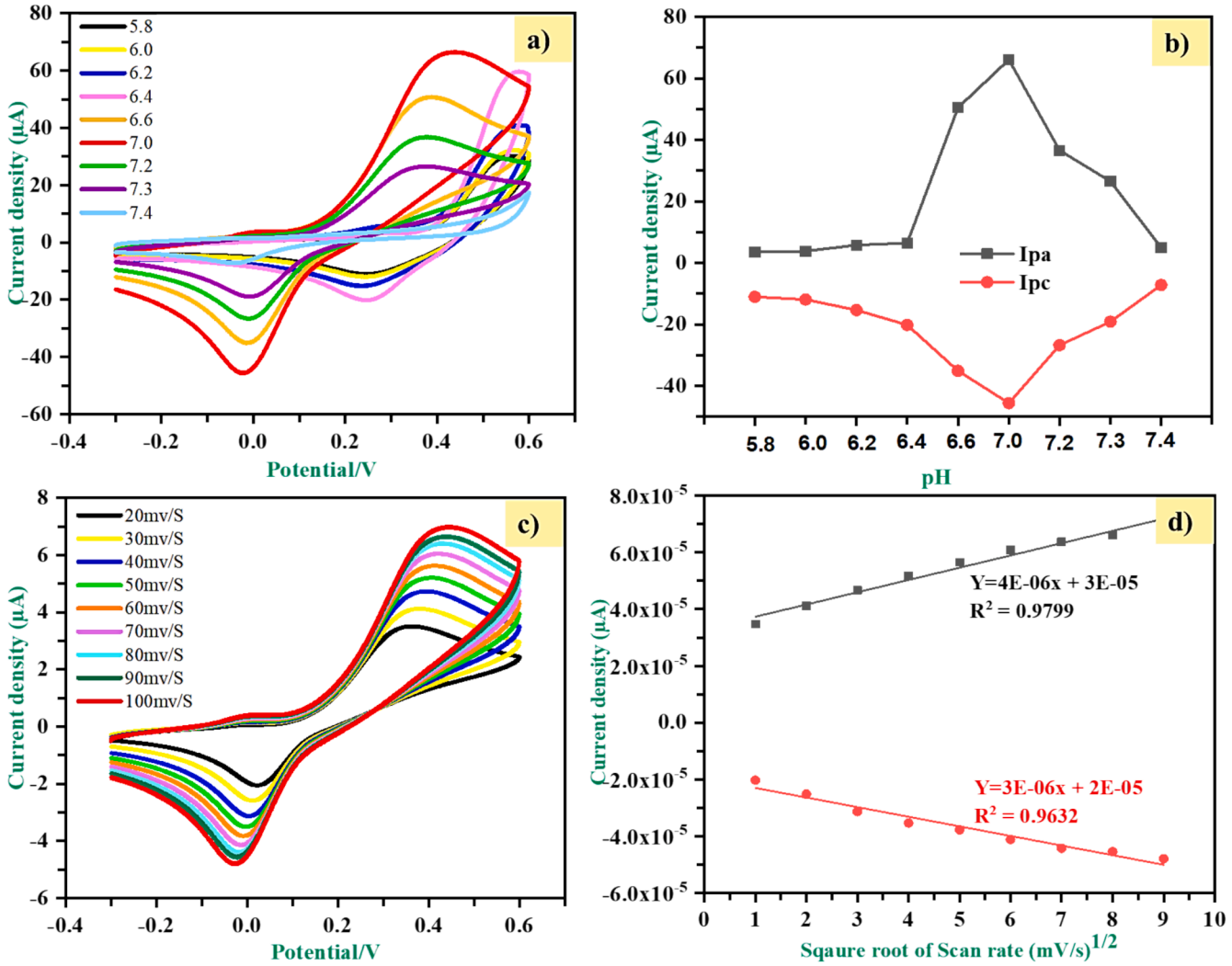

Fig. 15. (a) effect of pH on the redox response of modified electrode for catechol, (b) pH versus oxidation current of catechol,(c)Effect of scan rate on redox response in 40 µM catechol in PBS electrolyte pH 7, (d)plot of varied scan rate from 20 to 100 mV/s for current response.

Step 1: $C_6H_4(OH)_2$ (Catechol) $\xrightarrow{\text{Oxidation}}$ $C_6H_4(OH)\text{-}O\bullet + H^+ + e^-$ (Catechol radical)

Step 2: $C_6H_4(OH)\text{-}O\bullet \xrightarrow{\text{Oxidation}} C_6H_4(O\bullet)\text{-}O\bullet + H^+ + e^-$

Step 3: $C_6H_4(O\bullet)\text{-}O\bullet \xrightarrow{\text{Rearrangement}} C_6H_4O_2$ (Quinone)

Overall Reaction:

$C_6H_4(OH)_2 \xrightarrow{\text{Oxidation}} C_6H_4O_2 + 2H^+ + 2e^-$

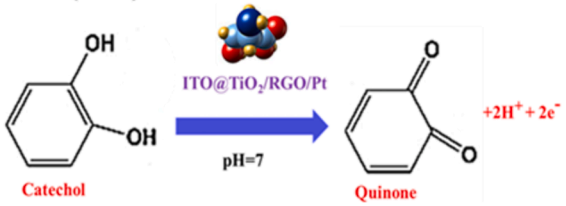

Scheme 1. The proposed mechanism for the oxidation of catechol on ITO@TiO_2 /RGO/Pt.

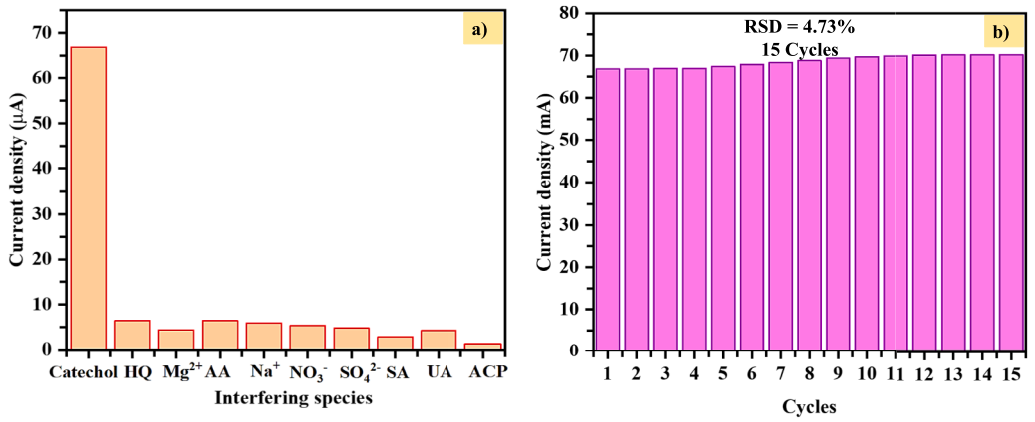

Fig. 16. (a) Effect of different interferants on redox response in 40 μM catechol in PBS electrolyte pH 7 at a scan rate of 100 mV/s, (b) stability of proposed ITO@TiO_2 /RGO/Pt.

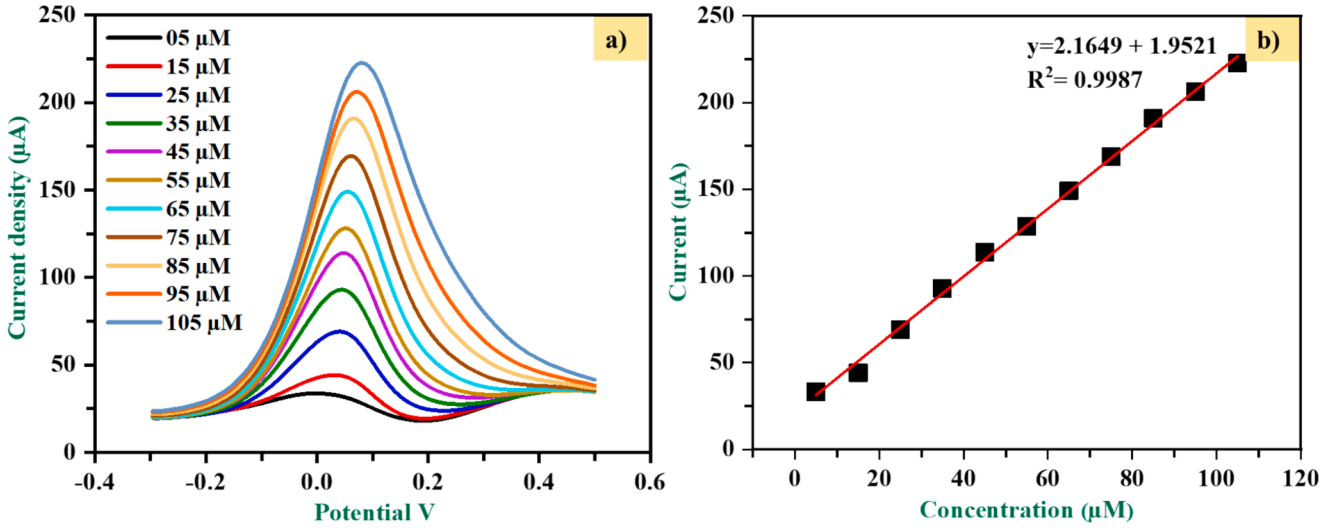

Fig. 17. (a)Calibration study at various concentrations of Catechol from 5 to 105 μM in PBS electrolyte pH 7, (b)plot of calibration with regression value R^2 = 0.9987.

Table 2
Comparison of prepared ITO@TiO_2 /RGO/Pt with reported sensors.

Electrodes	Techniques	LDR (μM)	LOD (μM)	References
PEDOT–CNT–Ty	CV	100–500	2.4	[57]
Co-ITO NCs	CV	1–200	01	[58]
SNGO composite	CV	10–320	0.28	[59]
Meso-Co_3O_4	CV, DPV	1–500	0.1	[60]
GO@PDA–AuNPs	DPV	0.3–67.55	0.015	[61]
ITO@TiO_2/RGO/Pt	DPV	05–105	0.013	This work

Table 3
Analytical applicability of ITO@TiO_2 /RGO/Pt in real water samples.

Sample	Added (μM)	Found (μM)	% Recovery
Mineral water	0	0	–
	5	4.90	98.0
	10	9.95	99.5
	15	15.2	101.3
Tap water	0	0	–
	5	4.96	99.2
	10	9.82	98.2
	15	14.56	97.1

5.3. Analytical application

The effectiveness of the ITO@TiO_2/RGO/Pt sensor was evaluated using various water samples, including tap water sourced from the National Centre of Excellence in Analytical Chemistry and mineral water from a local market. Each sample was tested in a 10 mL electrochemical cell with a 1:10 vol ratio of PBS electrolyte to water, using the standard addition method to determine unknown concentrations. Catechol concentrations of 5, 10, and 15 μM were added to the samples, and each concentration was tested four times. The recovery values for mineral water ranged from 98.0 % to 101.3 %, while those for tap water ranged from 97.1 % to 99.2 %, as detailed in Table 3. These results, all within acceptable limits, confirm the sensor's high analytical performance and reliability in detecting catechol in real water samples.

6. Limitations and future research

In summary, while the TiO_2/RGO/Pt nanocomposites show promise for various applications, addressing these limitations through rigorous research and testing is essential for confirming their practical viability and optimizing their performance. The exploration of TiO_2/RGO/Pt nanocomposites unveils significant limitations that must be addressed to

affirm their efficacy and applicability in real-world scenarios. These challenges encompass a range of factors, including complex material interactions influenced by synthesis methods and environmental conditions, which complicate the interpretation of their optical, structural, and electrochemical properties. Empirical validation is urgently needed, as many theoretical claims regarding photocatalytic performance and electron dynamics lack sufficient experimental support. Additionally, issues such as nanoparticle aggregation can adversely affect surface area and reactivity, while the stability of these materials under varying real-world conditions remains largely untested. Analytical techniques like FT-IR, EDX, XRD, and DLS provide useful insights, however, they are often insufficient in isolation, necessitating a comprehensive approach that employs multiple methods. Furthermore, results derived from controlled laboratory settings may not accurately reflect broader applications, and the long-term performance and recyclability of the catalysts require further investigation. Lastly, a deeper mechanistic understanding of the interactions among TiO_2, RGO, and Pt is crucial to unlocking their full potential. While the promise of TiO_2/RGO/Pt nanocomposites is evident, rigorous research and testing are essential to confirm their practical viability and optimize their performance for future applications.

7. Conclusion

In conclusion, the successful fabrication of an ITO@TiO_2/RGO/Pt electro-catalyst significantly advances electrochemical sensor technology for catechol detection. By employing the modified polyol process to prepare TiO_2/RGO/Pt nanocomposites and depositing them on ITO glass via drop-casting, we have created a highly sensitive sensor with exceptional electrocatalytic properties. The engineered TiO_2/RGO/Pt nanocomposites were subjected to characterization through several advanced analytical tools, which revealed their effective functionalities, morphology, elemental composition, and nanostructure, with an average size of 27.6 nm. The sensor demonstrated superior performance for catechol detection, with a wide linear range (5–105 μM), low detection limits (0.013 μM LOD, 0.046 μM LOQ), and excellent selectivity and stability in the presence of interfering agents. Real water sample analysis showed recovery rates of 97.1 % to 101.3 %, demonstrating its practical applicability for environmental monitoring. The sensor achieved over 7580 turnovers with a high TOF of 97.5 $mol•Catalyst^{-1}•min^{-1}$ further supports its potential for commercial-scale use. This work provides a robust and reliable method for the on-site detection of catechol, offering significant contributions to environmental safety and water quality monitoring.

Ethical approval

There is no human or animal study in this article.

Author Statement

I write on behalf of myself and all co-authors to confirm that the results reported in the manuscript are original and that neither the entire work nor any of its parts have been previously published. We certify that it is an original research article that includes authentic data that has not been submitted elsewhere for publication in any other journal, including the Internet.

CRediT authorship contribution statement

Rimsha Larik: Writing – original draft, Software, Methodology, Conceptualization. **Aamna Balouch:** Writing – review & editing, Supervision. **Esra Alveroğlu Durucu:** Writing – review & editing. **Hulya Silah:** Validation, Formal analysis. **Abdullah:** Visualization. **Muhammad Saqaf Jagirani:** Project administration. **Muhammad Yaqoob soomro:** Resources, Investigation.

Funding

There is no funding source for this publication.

Declaration of competing interest

The authors declare that they have no known competing financial interests or personal relationships that could have appeared to influence the work reported in this paper.

Acknowledgment

The authors are grateful to the National Centre of Excellence in Analytical Chemistry, University of Sindh, Jamshoro, Pakistan.

Appendix A. Supplementary material

Supplementary data to this article can be found online at https://doi.org/10.1016/j.mseb.2024.117966.

Data availability

The data that has been used is confidential.

References

[1] H. Luo, et al., Rapid and sensitive detection of bisphenol a based on self-assembly, Micromachines 11 (1) (2019) 41.
[2] A.U. Alam, M.J. Deen, Bisphenol A electrochemical sensor using graphene oxide and β-cyclodextrin-functionalized multi-walled carbon nanotubes, Anal. Chem. 92 (7) (2020) 5532–5539.
[3] N. Hareesha, et al., Electrochemically polymerized glutamine-activated graphite paste surface as a green biosensor for sensitive catechol detection in water samples, J. Mater. Sci. Mater. Electron. 34 (6) (2023) 533.
[4] E.I. Naik, et al., Design and fabrication of an innovative electrochemical sensor based on Mg-doped ZnO nanoparticles for the detection of toxic catechol, Mater. Chem. Phys. 281 (2022) 125860.
[5] C.C. Lobo, N.C. Bertola, E.M. Contreras, Stoichiometry and kinetic of the aerobic oxidation of phenolic compounds by activated sludge, Bioresour. Technol. 136 (2013) 58–65.
[6] M.N. Karim, J.E. Lee, H.J. Lee, Amperometric detection of catechol using tyrosinase modified electrodes enhanced by the layer-by-layer assembly of gold nanocubes and polyelectrolytes, Biosens. Bioelectron. 61 (2014) 147–151.
[7] M. Sittig, Handbook of Toxic and Hazardous Chemicals and Carcinogens, Second ed., Noyes Publications, Park Ridge NJ, 1985.
[8] Health, U.D.o. and H. Services, *Hazardous substances data bank (HSDB, online database)*. National Toxicology Information Program, National Library of Medicine, Bethesda, MD, 1993.
[9] H. Rao, et al., Gold nanoparticle/chitosan@ N, S co-doped multiwalled carbon nanotubes sensor: fabrication, characterization, and electrochemical detection of catechol and nitrite, ACS Sustain. Chem. Eng. 5 (11) (2017) 10926–10939.
[10] X. Liu, et al., Facile preparation of four-in-one nanozyme catalytic platform and the application in selective detection of catechol and hydroquinone, Sens. Actuat. B 337 (2021) 129763.
[11] C. Liu, et al., Surface-enhanced Raman scattering of phenols and catechols by a molecular analogue of titanium dioxide, Anal. Chem. 92 (8) (2020) 5929–5936.
[12] M.U. Hossain, M.T. Rahman, M.Q. Ehsan, Simultaneous detection and estimation of catechol, hydroquinone, and resorcinol in binary and ternary mixtures using electrochemical techniques, Int. J. Anal. Chem. 2015 (2015).
[13] L.-J. Zhao, et al., Electrocatalytic efficiency analysis of catechol molecules for NADH oxidation during nanoparticle collision, Anal. Chem. 88 (17) (2016) 8375–8379.
[14] A. Maikap, et al., A novel non-enzymatic zinc oxide thin film based electrochemical recyclable strip with device interface for quantitative detection of catechol in water, Biosens. Bioelectron. 128 (2019) 32–36.
[15] C. Ma, et al., Recent progress in electrochemiluminescence sensing and imaging, Anal. Chem. 92 (1) (2019) 431–454.
[16] W. Lv, et al., Recent advances in electrochemiluminescence-based simultaneous detection of multiple targets, TrAC Trends Anal. Chem. 123 (2020) 115767.
[17] A. Scozzari, Electrochemical sensing methods: A brief review, Algal Toxins: Nature, Occurrence, Effect and Detection (2008) 335–351.
[18] Y. Fu, et al., Nonenzymatic glucose sensor based on ITO electrode modified with gold nanoparticles by ion implantation, Electrochim. Acta 120 (2014) 314–318.
[19] H. Silah, et al., Modified indium tin oxide electrodes: electrochemical applications in pharmaceutical, biological, environmental and food analysis, TrAC Trends Anal. Chem. 141 (2021) 116289.
[20] E.B. Aydın, M. Aydın, M.K. Sezgintürk, Selective and ultrasensitive electrochemical immunosensing of NSE cancer biomarker in human serum using epoxy-substituted

poly (pyrrole) polymer modified disposable ITO electrode, Sens. Actuat. B 306 (2020) 127613.
[21] A.M. Mahar, et al., Fabrication of Pt-Pd@ ITO grown heterogeneous nanocatalyst as efficient remediator for toxic methyl parathion in aqueous media, Environ. Sci. Pollut. Res. 27 (2020) 9970–9978.
[22] G. Chang, et al., Gold nanoparticles directly modified glassy carbon electrode for non-enzymatic detection of glucose, Appl. Surf. Sci. 288 (2014) 524–529.
[23] S. Amin, et al., Recent trends in development of nanomaterials based green analytical methods for environmental remediation, Curr. Anal. Chem. 17 (4) (2021) 438–448.
[24] S.K. Tiwari, et al., Graphene research and their outputs: Status and prospect, J. Sci.: Adv. Mater. Devices 5 (1) (2020) 10–29.
[25] B. Aissa, et al., Recent progress in the growth and applications of graphene as a smart material: a review, Front. Mater. 2 (2015) 58.
[26] D. Verma, et al., Fabrication of a sensitive electrochemical sensor platform using reduced graphene oxide-molybdenum trioxide nanocomposite for BPA detection: an endocrine disruptor, J. Environ. Chem. Eng. 9 (4) (2021) 105504.
[27] C. Yu, et al., A disposable indium-tin-oxide sensor modified by gold nanorod–chitosan nanocomposites for the detection of H_2O_2 in cancer cells, Chem. Commun. 50 (55) (2014) 7329–7331.
[28] Y. Zhang, et al., In situ growth of Ag-reduced graphene oxide-carbon nanotube on indium tin oxide and its application for electrochemical sensing, Mater. Res. Bull. 84 (2016) 355–362.
[29] A. Parkash, et al., Synthesis and characterization of graphene oxide and its composites, ECS J. Solid State Sci. Technol. 11 (8) (2022) 081011.
[30] M.T. Shah, et al., Synthesis of magnetite nanoparticles and its application as electrode material for the electrochemical oxidation of methanol, J. Electron. Mater. 47 (2018) 5321–5333.
[31] N. Mukwevho, et al., Photocatalytic activity of $Gd_2O_2CO_3$ZnOCuO nanocomposite used for the degradation of phenanthrene, SN Appl. Sci. 1 (2019) 1–11.
[32] N. Hidayah, et al., Comparison on graphite, graphene oxide and reduced graphene oxide: Synthesis and characterization, AIP Publishing, 2017.
[33] R. Wang, et al., Synthesis and degradation kinetics of TiO2/GO composites with highly efficient activity for adsorption and photocatalytic degradation of MB, Sci. Rep. 9 (1) (2019) 18744.
[34] A.H. Pato, et al., Fabrication of TiO 2@ ITO-grown nanocatalyst as efficient applicant for catalytic reduction of Eosin Y from aqueous media, Environ. Sci. Pollut. Res. 28 (2021) 947–959.
[35] H. Jeong, et al., Tailoring the characteristics of graphite oxides by different oxidation times, J. Phys. D Appl. Phys. 42 (6) (2009) 065418.
[36] H. Zhang, et al., Synthesis and characterization of TiO 2/graphene oxide nanocomposites for photoreduction of heavy metal ions in reverse osmosis concentrate, RSC Adv. 8 (60) (2018) 34241–34251.
[37] M. Bera, P. Gupta, P.K. Maji, Facile one-pot synthesis of graphene oxide by sonication assisted mechanochemical approach and its surface chemistry, J. Nanosci. Nanotechnol. 18 (2) (2018) 902–912.
[38] M.N. Sepehr, et al., Surface modification of pumice enhancing its fluoride adsorption capacity: an insight into kinetic and thermodynamic studies, Chem. Eng. J. 228 (2013) 192–204.
[39] S. Zolghadr, S. Kimiagar, A. Davarpanah, Magnetic property of $\alpha $-$Fe_2O_3$–GO nanocomposite, IEEE Trans. Magn. 53 (12) (2017) 1–6.
[40] A.T. Habte, D.W. Ayele, Synthesis and characterization of reduced graphene oxide (rGO) started from graphene oxide (GO) using the tour method with different parameters, Adv. Mater. Sci. Eng. 2019 (2019).
[41] E. Andrijanto, et al., Facile synthesis of graphene from graphite using ascorbic acid as reducing agent, AIP Publishing, 2016.
[42] E. Alsharaeh, et al., Sol-gel-assisted microwave-derived synthesis of anatase Ag/TiO_2/GO nanohybrids toward efficient visible light phenol degradation, Catalysts 7 (5) (2017) 133.
[43] N. Lertthanaphol, et al., One-step hydrothermal synthesis of precious metal-doped titanium dioxide-graphene oxide composites for photocatalytic conversion of CO_2 to ethanol, ACS Omega 6 (51) (2021) 35769–35779.
[44] P. Ribao, M.J. Rivero, I. Ortiz, TiO_2 structures doped with noble metals and/or graphene oxide to improve the photocatalytic degradation of dichloroacetic acid, Environ. Sci. Pollut. Res. 24 (2017) 12628–12637.
[45] S.-F. Wang, Y.-F. Hsu, Y.-S. Lee, Microstructural evolution and optical properties of doped TiO_2 films prepared by RF magnetron sputtering, Ceram. Int. 32 (2) (2006) 121–125.
[46] N. Durán, W.J. Fávaro, Nanopharmaceuticals and their applications in bladder cancer therapy: a mini review, J. Braz. Chem. Soc. 29 (2018) 973–981.
[47] A.K. Patlolla, et al., Toxicity evaluation of graphene oxide in kidneys of Sprague-Dawley rats, Int. J. Environ. Res. Public Health 13 (4) (2016) 380.
[48] I.S. Grover, S. Singh, B. Pal, The preparation, surface structure, zeta potential, surface charge density and photocatalytic activity of TiO_2 nanostructures of different shapes, Appl. Surf. Sci. 280 (2013) 366–372.
[49] P. Pandi, C. Gopinathan, Synthesis and characterization of TiO_2–NiO and TiO_2–WO_3 nanocomposites, J. Mater. Sci. Mater. Electron. 28 (2017) 5222–5234.
[50] A. Mikolajczyk, et al., Zeta potential for metal oxide nanoparticles: a predictive model developed by a nano-quantitative structure–property relationship approach, Chem. Mater. 27 (7) (2015) 2400–2407.
[51] M.L. Pedersen, et al., Investigation of surface energy, wettability and zeta potential of titanium dioxide/graphene oxide membranes, J. Photochem. Photobiol. A Chem. 366 (2018) 162–170.
[52] S. Gurunathan, et al., Oxidative stress-mediated antibacterial activity of graphene oxide and reduced graphene oxide in pseudomonas aeruginosa, Int. J. Nanomed. (2012) 5901–5914.
[53] V. Keerthana, et al., Synthesis, characterization and applications of GO–TiO_2 nanocomposites in textile dye remediation, Iran. J. Sci. Technol., Trans. a: Sci. 46 (4) (2022) 1149–1161.
[54] G. Chen, B. Fang, Preparation of solid acid catalyst from glucose–starch mixture for biodiesel production, Bioresour. Technol. 102 (3) (2011) 2635–2640.
[55] N. Tsubouchi, C. Xu, Y. Ohtsuka, Carbon crystallization during high-temperature pyrolysis of coals and the enhancement by calcium, Energy Fuel 17 (5) (2003) 1119–1125.
[56] K.A. Castro, et al., Galactodendritic porphyrinic conjugates as new biomimetic catalysts for oxidation reactions, Inorg. Chem. 54 (9) (2015) 4382–4393.
[57] C. Lete, et al., Multi-analyte determination of dopamine and catechol at single-walled carbon nanotubes–Conducting polymer–Tyrosinase based electrochemical biosensors, J. Electroanal. Chem. 744 (2015) 53–61.
[58] S. Premlatha, G.R. Bapu, Direct current electrodeposition of Co-ITO nanoflakes modified steel electrode for highly selective non enzymatic detection of catechol, J. Alloy. Compd. 767 (2018) 622–631.
[59] Y. Qi, et al., Facile synthesis of 3D sulfur/nitrogen co-doped graphene derived from graphene oxide hydrogel and the simultaneous determination of hydroquinone and catechol, Sens. Actuat. B 279 (2019) 170–176.
[60] S. Cui, et al., Mesoporous cobalto-cobaltic oxide modified glassy carbon electrode for simultaneous detection of hydroquinone and catechol, J. Electroanal. Chem. 782 (2016) 225–232.
[61] S. Palanisamy, et al., Preparation and characterization of gold nanoparticles decorated on graphene oxide@ polydopamine composite: application for sensitive and low potential detection of catechol, Sens. Actuat. B 233 (2016) 298–306.